

SIMULATING NONLINEAR COSMOLOGICAL STRUCTURE FORMATION WITH MASSIVE NEUTRINOS

ARKA BANERJEE & NEAL DALAL

Department of Physics, University of Illinois at Urbana-Champaign, 1110 West Green Street, Urbana, IL 61801-3080 USA
Draft version July 28, 2016

ABSTRACT

We present a new method for simulating cosmologies that contain massive particles with thermal free streaming motion, such as massive neutrinos or warm/hot dark matter. This method combines particle and fluid descriptions of the thermal species to eliminate the shot noise known to plague conventional N-body simulations. We describe this method in detail, along with results for a number of test cases to validate our method, and check its range of applicability. Using this method, we demonstrate that massive neutrinos can produce a significant scale-dependence in the large-scale biasing of deep voids in the matter field. We show that this scale-dependence may be quantitatively understood using an extremely simple spherical expansion model which reproduces the behavior of the void bias for different neutrino parameters.

1. INTRODUCTION

One of the central tenets of the standard cosmological model is that structure observed in the present universe formed via gravitational evolution of initially linear density perturbations which arose in the primordial universe (Peebles 1980; Dodelson 2003). The initially linear perturbations responsible for producing anisotropies in the cosmic microwave background (Planck Collaboration et al. 2014) are expected to eventually develop into nonlinear cosmological structures like halos and filaments at low redshift (Mo et al. 2010). Predicting the nonlinear evolution of cosmic structure has been a numerically challenging problem for many years. The method of choice for computing structure formation has been N-body simulation. The accuracy and efficiency of this method have been well established for standard Λ CDM cosmologies (Heitmann et al. 2005, 2008). These simulations have been used to study many aspects of structure formation, including the mass functions (Jenkins et al. 2001; Tinker et al. 2008; Warren et al. 2006) and profiles (Navarro et al. 1997; Colberg et al. 2005; Zemp 2009; Diemand et al. 2008; Diemand & Moore 2011; Springel et al. 2008; Stadel et al. 2009) of halos and voids, and their large scale clustering (e.g. Springel et al. 2005; Gao et al. 2005; Tinker et al. 2008, 2010).

Although N-body simulations have been enormously successful in describing the evolution of Λ CDM cosmologies, they have not fared as well for studying certain other cosmologies, especially universes containing massive particles with large thermal velocities in the initial phase space distribution of the species. The large thermal velocities of these particles generate spurious structures in the density field due to discreteness effects inherent in N-body methods, as the particles stream large distances in random directions. At scales below this streaming scale, the density distribution of the simulation particles follows a Poisson shot noise distribution, instead of the correct, physical density. The power spectrum at large wavenumber would then be given by $P(k) \sim \bar{n}^{-1}$, where \bar{n} is the mean density of particles in the simulation. For

typical values of \bar{n} , the shot noise power spectrum can completely dominate the physical power spectrum (which is damped on these scales by the streaming motions), leading to spurious structures forming everywhere in the simulation volume. Therefore, improvements in numerical methods are essential to develop a reliable and consistent method for studying structure formation in such cosmologies.

An example of a cosmology with fast moving massive particles is our own universe, which is known to contain massive neutrinos. Neutrinos are among the most abundant particles in the universe, comparable to photons in terms of their number density (Dodelson 2003). Oscillation experiments have clearly established that at least two neutrino states are massive, and these experiments have also placed tight bounds on the mass differences between the three mass eigenstates of neutrinos (Fukuda et al. 1998; Ahmad et al. 2001; Ahn et al. 2006; Eguchi et al. 2003; An et al. 2012). Even though the absolute masses are not yet known, the mass splittings imply that at least one of the species is as heavy as ~ 0.06 eV. Given the current cosmic neutrino background temperature $T_\nu \sim 1.68 \times 10^{-4}$ eV (Dodelson 2003), this means that this species is highly non-relativistic today, and can therefore gravitationally cluster. The effects of massive neutrinos on large-scale structure are well-understood on large scales and at early times, when fluctuations are in the linear regime (Lesgourgues & Pastor 2014). However, at late times and smaller scales, density fluctuations become non-linear, rendering linear perturbation theory calculations invalid.

Different groups have put forward different approaches to attacking this problem. Brandbyge & Hannestad (2009) and Archidiacono & Hannestad (2016) have proposed treating the neutrinos as a linear fluid on a grid coupled to the fully non-linear, N-body evolution of the cold dark matter (CDM) particles. Similarly, Ali-Haïmoud & Bird (2013) suggested solving the linearized Boltzmann equations for neutrinos coupled to the N-body evolution of CDM particles. By their very nature, these quasi-linear methods break down when the overdensities in the neutrino fluid approach $\mathcal{O}(1)$. At late times, massive neutrinos can become cold enough to

be captured into the deepest potential wells in the simulations - the largest halos. The overdensities of neutrinos in these halos can be significantly larger than $\mathcal{O}(1)$, limiting the validity of linearized methods at late times.

Another method which has been proposed is to treat the neutrinos as a different species of particles with different mass than CDM particles in a normal N-body simulation at all redshifts (Villaescusa-Navarro et al. 2014). A related method is to use the linear treatment for neutrinos at early redshifts, but then to switch to N-body treatment once perturbations in the neutrino fluid become non-linear (Brandbyge & Hannestad 2010). While traditional N-body methods suffer from the shot noise issue mentioned above, these authors argue that since the neutrinos constitute a small part of the energy budget ($\Omega_\nu \ll 1$), their effects are always subdominant to CDM, and the shot noise effect is not strong enough to significantly alter structure formation. On the other hand, since shot noise can be significant compared to the real physical clustering of neutrinos in the simulation, this means that calculations of neutrino effects on the power spectrum can suffer from large *fractional* errors, even if the absolute errors on the power spectrum are small thanks to the small mass fraction in neutrinos. Given that the point of performing such simulations is the precise calculation of neutrino effects, the fractional error on neutrino effects may be a more relevant metric than the absolute error on the total power spectrum. A number of interesting results have been found using these methods (Villaescusa-Navarro et al. 2011, 2013; Brandbyge et al. 2010; Castorina et al. 2014; Costanzi et al. 2013; Inman et al. 2015; Castorina et al. 2015; Carbone et al. 2016). However, with future cosmological surveys expected to reduce error bars on multiple observables significantly, an improvement in the accuracy of neutrino simulations may now be warranted.

Similarly, besides neutrinos, dark matter particles can also have significant random thermal velocities, depending on the DM temperature at freezeout. It has been suggested that Warm Dark Matter (Bode et al. 2001) can alleviate certain small-scale problems present for CDM universes, like the core-cusp problem of halo profiles (de Blok et al. 2008; de Blok 2010) and the missing satellite problem (Moore et al. 1999; Klypin et al. 1999; Diemand et al. 2008; Springel et al. 2008). If DM particles have a finite thermal velocity dispersion, then those particles will randomly stream a finite distance, and this random streaming acts to suppress structure on scales below the free-streaming length. The streaming length of WDM particles is much smaller than the streaming length of neutrinos (Bode et al. 2001; Villaescusa-Navarro & Dalal 2011), and if the simulations are initialized in a way that the particles have random thermal velocities, the scales affected by shot noise would be smaller than in neutrino simulations. We refer to these sort of simulations as “hot start” simulations. However, since the WDM is the dominant component in these simulations, any amount of shot noise coming from the thermal velocities is sufficient to seed the formation of spurious structures. “Hot start” N-body simulations are therefore not an accurate method for studying such WDM cosmologies.

To get around this problem, the “cold start” method has typically been used in the literature

(Avila-Reese et al. 2001; Wang & White 2007). In this method, the random thermal velocities of particles are *not* included in the simulation initial conditions. To account for the damping of the power spectrum, this method initializes using the linear power spectrum for the WDM species at redshift $z = 0$, scaled back to the starting redshift of the simulation using CDM growth factors. This method therefore necessarily does not capture the spatial dependence and time dependence of the growth of structure, but it *does* eliminate artifacts arising from random thermal velocities. Nonetheless, the cold start method suffers from its own artifacts, like the “beads on a string” phenomenon (Wang & White 2007). Angulo et al. (2013) have proposed an interesting method to eliminate these “beads on a string” artifacts and other spurious structures from WDM simulations. Their method employs a tetrahedral tessellation of the 6-dimensional phase space of simulation particles to follow the evolution of the WDM densities. However, it is not yet clear if this method is accurate inside collapsed and virialized regions such as halos or subhalos, whose abundance will likely provide stringent constraints on WDM models in upcoming years (e.g. Hezaveh et al. 2013, 2016). Alternatively, Hobbs et al. (2016) have proposed that adaptive softening of the gravitational force can help to suppress spurious structure found in cold start simulations of WDM cosmologies.

In this paper, we present a novel method to simulate cosmologies with hot particles which is valid at all redshifts, in both linear and non-linear regimes. This method makes use of both particle techniques from N-body simulations as well as hydrodynamic techniques from fluid simulations. This paper is arranged as follows. In §2, we derive the relevant equations of motion for hot species in an expanding universe. We describe the implementation of our method at early and late redshifts in §3. In §4 we discuss the time integration techniques for the particles in our simulations, as well the hydrodynamic scheme we implement. In §5, we discuss a number of tests, in both the linear as well as the non-linear regime to validate our code. We use this method to show a novel effect in void biasing with neutrinos in §6. Finally, we list our main conclusions and directions for future work in §7.

2. EQUATIONS OF MOTION

In this section, we review the equations of motion governing hot species in an expanding universe. We take moments of the Boltzmann equation to derive effective fluid equations that allow us to evolve the hot species using hydrodynamic methods.

2.1. Collisionless Boltzmann equation

For the applications we are interested in, we consider the WDM and neutrinos to be essentially collisionless, and our starting point will be the collisionless Boltzmann equation

$$\frac{df}{dt} = \frac{\partial f}{\partial t} + \frac{\partial f}{\partial x^i} \frac{dx^i}{dt} + \frac{\partial f}{\partial p^i} \frac{dp^i}{dt} = 0 \quad (1)$$

where $f(\mathbf{x}, \mathbf{p})$ is the phase space distribution function of the dynamical species in the simulation volume. Working in Newtonian gauge with the Newtonian potentials Φ and

Ψ , which are typically of order 10^{-5} in units where $c = 1$, we have up to first order in the potentials (Dodelson 2003)

$$\frac{dx^i}{dt} = \frac{p^i}{aE} (1 - \Phi + \Psi). \quad (2)$$

In equation (2), $E = \sqrt{p^i p^i + m^2}$ and a is the scale factor. Similarly,

$$\frac{dp^i}{dt} = -p^i \frac{\partial \Phi}{\partial t} - p^i \frac{\dot{a}}{a} - \frac{E}{a} \frac{\partial \Psi}{\partial x^i} \quad (3)$$

to first order in the potentials. Here \dot{a} means a derivative with respect to time, and not a conformal time derivative. Substituting (2) and (3) into (1) we have

$$\begin{aligned} \frac{\partial f}{\partial t} + \frac{\partial f}{\partial x^i} \left[\frac{p^i}{aE} (1 - \Phi + \Psi) \right] \\ + \frac{\partial f}{\partial p^i} \left[-p^i \frac{\partial \Phi}{\partial t} - p^i \frac{\dot{a}}{a} - \frac{E}{a} \frac{\partial \Psi}{\partial x^i} \right] = 0. \end{aligned} \quad (4)$$

2.2. Poisson equation

The metric potentials Φ and Ψ are related to the matter content via the Poisson equation. Since we are interested in epochs during matter domination ($z \lesssim 300$) when the overall anisotropic stress is small, we can assume $\Psi = -\Phi$. In Newtonian gauge, we have

$$\nabla^2 \Psi = 4\pi G a^2 \left[\bar{\rho} \delta - 3 \frac{\dot{a}}{a} (1+w) \partial_i v^i \right] \quad (5)$$

where v_i is the local peculiar velocity, $\delta = \delta\rho/\bar{\rho}$ is the local overdensity, and $w = \bar{P}/\bar{\rho}$ is the background equation of state. All of these fluid quantities will be defined formally in terms of moments of the distribution function below. For simulation boxes where the volume is much smaller than the Hubble volume, the second term in the brackets on the right hand side of eqn. (5) can be neglected.

2.3. Obtaining the Boltzmann moment equations

We can use the Boltzmann equation (1) to derive fluid equations for collisionless particles by integrating over various moments. First, we derive the continuity equation in the usual way, by multiplying (4) by E and integrating over momentum. We define the real-space density in terms of the phase space density in the following manner,

$$\rho(\mathbf{x}) = \int E f(\mathbf{x}, \mathbf{p}) d^3 \mathbf{p} \quad (6)$$

Since we are interested in the relative density contrast $\delta = (\rho - \bar{\rho})/\bar{\rho}$, we can cast the continuity equation into an equation for the time evolution of δ :

$$\begin{aligned} \dot{\delta} = -\frac{1}{a} \frac{\partial}{\partial x^i} \left[(1 + 2\Psi) \Pi^i \right] - 3\dot{\Phi} (1 + \delta) (1 + W) \\ - 3 \frac{\dot{a}}{a} (1 + \delta) (W - w). \end{aligned} \quad (7)$$

where $w = \bar{P}/\bar{\rho}$ is the background equation of state and we have defined

$$\Pi^i(\mathbf{x}) = \frac{\int p^i f(\mathbf{x}, \mathbf{p}) d^3 \mathbf{p}}{\bar{\rho}} \quad (8)$$

and

$$W(\mathbf{x}) = \frac{\int \frac{p^i p^i}{3E} f(\mathbf{x}, \mathbf{p}) d^3 \mathbf{p}}{\rho(\mathbf{x})}. \quad (9)$$

If the species is non-relativistic, the bulk velocity can be simply defined as

$$v^i(\mathbf{x}) = \frac{\Pi^i(\mathbf{x})}{1 + \delta(\mathbf{x})} \quad (10)$$

In eqn. (7), the last two terms on the right hand side are typically small compared to the first term. Since we are interested in matter domination regimes, $\dot{\Phi}$ is small compared to the spatial derivatives of Φ , and we can neglect the second term on the RHS without a loss of accuracy. If the particles are relativistic, the last term is small or zero because the local sound speed and the background sound speeds are the same, and $(W - w)$ vanishes. When particles are non-relativistic, W and w are individually small ($\sim 10^{-6}$) and even in non-linear regimes the last term remains much smaller than the first term.

Next we multiply eqn. (4) by p^i and integrate to get the Euler equation for the fluid

$$\begin{aligned} \dot{\Pi}^i = -(1 - 3w) \frac{\dot{a}}{a} \Pi^i - \frac{1}{a} \frac{\partial}{\partial x^j} \left[(1 + \delta) W^{ij} \right] \\ - \frac{1 + \delta}{a} \frac{\partial \Psi}{\partial x^i} \end{aligned} \quad (11)$$

with

$$W^{ij}(\mathbf{x}) = \frac{\int \frac{p^i p^j}{E} f(\mathbf{x}, \mathbf{p}) d^3 \mathbf{p}}{\rho(\mathbf{x})} \quad (12)$$

Note that, in principle, we can continue this procedure of generating equations using higher and higher moments of the Boltzmann equation. Each equation will be coupled to the next - this is apparent by looking at the structure of the two equations we have derived, (7) and (11). In the next section, we comment on how we close this infinite hierarchy of equations.

2.4. SPH equations

As we will show in §5, there are some situations in which it is advantageous to use a Lagrangian description of the fluid rather than an Eulerian description. We use a Smoothed Particle Hydrodynamics (SPH) approach for these problems, following the procedures in Monaghan (1992). For non-relativistic collisionless particles, the equations of motion can be written as

$$\frac{dx^i}{dt} = \frac{v^i}{a} (1 - \Phi + \Psi) \quad (13)$$

and

$$\begin{aligned} \frac{dv^i}{dt} = -v^i \frac{\partial \Phi}{\partial t} - v^i \frac{\dot{a}}{a} - \frac{1}{a} \frac{\partial \Psi}{\partial x^i} \\ - \frac{1}{(1 + \delta) a} \frac{\partial \left[(1 + \delta) W^{ij} \right]}{\partial x^j}. \end{aligned} \quad (14)$$

3. CLOSING THE HIERARCHY

To study the evolution of the collisionless fluid with the above equations, we need some way to close the Boltzmann hierarchy. For collisional fluids, one can use an equation of state to relate the energy density and the pressure to close the system of equations. However, in the collisionless cases that we will be interested in (neutrinos and WDM) there is no simple equation of state, and so an alternative closure method is required.

To motivate our method to close the Boltzmann hierarchy, it will be useful to consider the approach used in particle-mesh (PM) N-body simulations (Hockney & Eastwood 1988). In N-body simulations, Lagrangian particles are evolved under the influence of their collective gravitational field. Those particles represent a Monte Carlo sampling of the distribution function, and in PM simulations, those particles are used to estimate the density field $\delta(\mathbf{x})$ that enters Eqn. (5). In effect, PM simulations use particles to close the Boltzmann hierarchy at its zeroth moment. In principle, however, we could use those particles to estimate other quantities that enter the fluid equations. For example, we could use particles to estimate a bulk fluid velocity, and then use that estimated velocity to evolve the density field using the continuity equation (7). Alternatively, we could use particles to estimate a stress tensor entering the Euler equation (11) that would truncate the hierarchy at its 2nd moment. Indeed we can estimate an arbitrary moment of the distribution function from particles, and truncate the Boltzmann hierarchy accordingly.

Therefore, the method we use is the following. We represent the collisionless fluid (e.g. neutrinos or WDM) simultaneously using fluid quantities on a grid and using test particles as well. We evolve the grid fluid using fluid equations like (7) and (11), and we truncate the Boltzmann hierarchy of fluid equations using moments of the distribution function estimated from the test particles, e.g. Eqn. (8) or (12). The test particles evolve under the gravitational field estimated from the fluid, i.e. Eqns. (2) and (3). Compared to traditional PM simulations, our approach involves solving more equations than the Poisson equation (i.e. fluid equations), and involves estimating higher moments of the particle distribution function (i.e. 3 components of the bulk velocity, or 6 components of the stress tensor, rather than a single scalar density field). This would appear to be considerably more expensive than traditional PM codes, but as we argue below, the benefits of using this approach in certain situations can outweigh the added costs.

3.1. Early evolution

We initialize our simulations using perturbation theory. We use Eulerian PT to initialize fluid quantities on the grid, and Lagrangian PT to initialize the test particles. In addition to the LPT velocities, the test particles are also given random thermal velocities drawn from the distribution function of the species we are interested in.

At early times, the particles can have large thermal velocities. These random thermal velocities can produce shot noise in any quantity we try to estimate from the particles, in the same way that the shot noise in particle positions generates noise in the density field computed from the particles, as discussed in the introduction. One

difference between the shot noise in particle velocities, compared to the noise in particle positions, is that the velocity noise diminishes over time as the universe expands. This means that shot noise in fluid quantities like the bulk velocity or velocity dispersion becomes small at low redshift, in contrast to the shot noise in the estimated density field. This illustrates one reason why it can be advantageous to estimate quantities other than the density from the particles.

Nevertheless, at early times the shot noise in velocities is large. In principle, this can be suppressed by increasing the number of particles in the simulation, but in many cases of interest, the required number of particles is orders of magnitude too large to be feasible. Therefore, using more particles in the simulation is not a practical solution in most situations of interest.

Another way to effectively increase the number of particles used in estimating fluid quantities is to spatially smooth those quantities. Spatially smoothing the fluid quantities is equivalent to estimating those quantities at a point using a larger volume, and hence more particles. The obvious reason why simulations normally do not spatially smooth over large volumes to suppress shot noise is that smoothing erases any small-scale structure in the estimated quantities. For species like cold dark matter, there is structure on all spatial scales, and so spatially smoothing would incorrectly eliminate real physical structure in the DM distribution. However, for the hot species of interest to us, the high temperature implies that there is a Jeans scale $k_J \sim aH/c_s$ below which small-scale structure is actively suppressed. Arguably, therefore, spatially smoothing is not necessarily invalid as long as the smoothing length is always safely below the Jeans scale.

On the other hand, the power spectrum does not vanish at $k > k_J$. Since we would like to accurately evolve the power spectrum on all scales in the simulation, including scales below the Jeans scale, this restricts what fluid quantities we can spatially smooth. For example, we cannot use the smoothing technique to estimate the velocity field, because this will extinguish the growth of structure on all scales below the smoothing scale. This becomes apparent if one looks at the linear continuity equation in Fourier space:

$$\dot{\delta}_k = -\frac{i\mathbf{k}\cdot\mathbf{v}_k}{a} \quad (15)$$

Smoothing sets \mathbf{v}_k to 0 for $k > k_{\text{smoothing}}$, which gives the unphysical result $\dot{\delta}_k = 0$.

However, from our tests, we find that we *can* spatially smooth the velocity dispersion W^{ij} at early times without sacrificing accuracy. To see this, note that when the thermal velocities are large enough to require spatial smoothing to suppress shot noise, then the Jeans scale is large, and so structure in the hot species remains linear. Under the fluid approximation, fluctuations in the velocity dispersion are second order, however, since they involve two perturbed velocities. Therefore, spatially smoothing the velocity dispersion only drops second order fluctuations in the fluid approximation, and does not affect the linear evolution of the velocity field in the Euler equation (11). This breaks down when structure in the hot species becomes nonlinear, but in order

for structure to become nonlinear, the thermal velocities must be small, eliminating the need for spatial smoothing to suppress shot noise. Therefore, at all redshifts, we can estimate fluid quantities without significant thermal shot noise.

In order for this method to work, we must pick a sensible smoothing length. If the smoothing length is too small, shot noise will corrupt the evolution of fluid quantities, whereas if the smoothing length is too large (exceeding the Jeans scale), then spatial smoothing artificially removes real physical structure in the simulation. We set the smoothing length using the following argument. The quantity we are estimating from the particles is the velocity dispersion, and we require that the error in our estimate of the dispersion to be small compared to velocities generated by gravity. We estimate the dispersion at every point on the grid by evaluating

$$W^{ij}(\mathbf{x}) = \frac{\sum_{\mathbf{x}} \frac{p^i p^j}{E}}{\sum_{\mathbf{x}} E} - \frac{\sum_{\mathbf{x}} p^i}{\sum_{\mathbf{x}} E} \frac{\sum_{\mathbf{x}} p^j}{\sum_{\mathbf{x}} E} \quad (16)$$

where $\sum_{\mathbf{x}}$ stands for the sum over all particles at position \mathbf{x} . Note that for non-relativistic particles, E for every particle is approximately the mass, and so the denominators in the above expression count the total mass of particles at a given point. We use a cloud in cell (CIC) scheme to evaluate the different sums. The average thermal velocity dispersion is given by the equation of state w . Therefore, if N particles have been used to estimate the velocity dispersion, the error in the estimate will be $\Delta = w/\sqrt{N}$. The error is going to be small if Δ is small compared to the average velocity dispersion sourced by gravity (v_{esc}^2). The latter can be estimated by evaluating the average of the magnitude of the gravitational potential in the box, $|\Phi_{rms}|$. If we set $\Delta = \epsilon |\Phi_{rms}|$ for some error tolerance $\epsilon \ll 1$, then the number of particles that are needed to achieve the error tolerance is

$$N = \frac{w^2}{\epsilon^2 |\Phi_{rms}|^2}. \quad (17)$$

When structure is linear, we know that n , the average number of particles per pixel, is a good estimate of the actual number of particles per pixel (modulo shot noise). This means that we have

$$N = nV_s \approx nL_s^3 \quad (18)$$

where $V_s \propto L_s^3$ is the smoothing volume required. This gives us an expression for the smoothing length

$$L_s = \left(\frac{w^2}{\epsilon^2 |\Phi_{rms}|^2 n} \right)^{1/3}. \quad (19)$$

We can adjust ϵ and n to ensure that our smoothing length never exceeds the local Jeans scale calculated in linear theory. We also need to adjust our parameters so that we are no longer smoothing when non-linear structures like halos start forming in the simulation volume. At early times, the particles are hot (large w) and the smoothing length is large. As time progresses, the particles become colder, which means w decreases. At the same time, structure starts forming in the box and $|\Phi_{rms}|$ increases with time. These effects together mean that the smoothing length is a rapidly decreasing function of time.

3.2. Late evolution

As the simulation proceeds, the smoothing length reduces below a pixel at some redshift. The random motions of particles at redshifts after this time do not produce levels of shot noise which will affect the evolution of the power spectrum. Once the shot noise becomes negligible, we do not need to spatially smooth the fluid quantities. At subsequent times, our fluid approach may appear unnecessary, given the computational costs associated with our method compared to traditional N-body methods. Unfortunately, we cannot switch from fluid evolution to N-body even when the smoothing length is less than 1 pixel. The reason is that the particle density field has shot noise in it even at late time, arising from the motion of the particles at higher redshifts. Using the density field for further evolution would mean that structure induced by this shot noise would grow gravitationally, and would start forming spurious halos at lower redshifts. This means that even at later times, the density field of the particles should not be used directly to source gravity.

However, we can safely switch from estimating the velocity dispersion and evolving the fluid density and bulk velocity fields, to estimating the bulk velocity field and only evolving the density field using the continuity equation (7). This is safe at late times because we are not spatially smoothing the estimated velocity field. Switching from estimating dispersion to estimating velocity produces a considerable speed-up in the simulation, since fewer quantities are being estimated (3 velocities vs. 6 dispersions) and fewer fluid equations need to be evolved (only continuity, not Euler). To estimate bulk velocities on the grid from the positions and velocities of the particles, we once again use a CIC interpolation scheme,

$$u^i(\mathbf{x}) = \frac{\sum_{\mathbf{x}} p^i}{\sum_{\mathbf{x}} E}. \quad (20)$$

As noted above, switching to velocity estimation speeds up the code significantly. We have verified that we obtain consistent simulation results using the faster velocity estimation and the slower dispersion estimation at late times. Therefore, in all of our Eulerian simulations below, we will switch to velocity estimation once the smoothing length shrinks to below one pixel.

3.3. Smoothing in SPH simulations

We will show below in §5 that in certain cases, it can be advantageous to use a Lagrangian formulation of the fluid equations rather than an Eulerian description. The Lagrangian description we will use in those cases is smoothed particle hydrodynamics (SPH). In those simulations, we use the following technique. We use two sets of particles - the first set evolves following the SPH equations of motion Eqs. (13), (14), and a second set of test particles which are evolved using Eqs. (2), (3). Like in the Eulerian case, the test particles are given thermal velocities drawn from their Fermi-Dirac distributions. Once again, these particles are not used in any of the density estimates, but only used to measure the velocity dispersion on a grid, as defined in Eqn. (16). Such an estimate of the velocity dispersion will be plagued by shot noise at early times, and needs to be smoothed, and this is done following the same prescription for the smooth-

ing length discussed in §3.1. Given the smoothed velocity dispersions on a grid, we interpolate from the grid to the positions of individual SPH particles to assign velocity dispersions to them. Once the thermal dispersions have been assigned, we use standard cubic spline interpolations from Monaghan (1992) to measure the density and the velocity dispersion gradient required in Eq. (14). For example, the density the position of the a -th particle is given by (Monaghan 1992)

$$\rho(\mathbf{r}_a) = \sum_b m_b W(\mathbf{r}_a - \mathbf{r}_b, h) \quad (21)$$

where the sum runs over all other particles, W is the interpolation kernel, and h is the spline smoothing length, which we choose to be one grid cell. Notice that this spline smoothing length is different from the smoothing length we defined in Eq. (19).

Once the smoothing length from Eq. (19) falls below our force resolution on the grid, we start treating the SPH particles as standard N-body particles for the rest of the evolution, as the effects of their thermal velocities beyond that point is below the resolution of the simulation. In practice, this means that we use Eqs. (2), (3) for time evolution.

Our technique does not make full use of the capabilities of SPH, as we use an intermediate grid to find and smooth the velocity dispersions from the test particles. This automatically limits the resolution of the SPH technique, but since our objective was only to suppress the shot noise from thermal velocities and given that our gravitational force resolution is also limited by the same grid, the above method is sufficient for the purposes of our simulations.

4. INTEGRATION TECHNIQUES

4.1. Particle time integration

For the test particles we use in the simulations, as well as for CDM particles in neutrino simulations, we use the standard Kick-Drift-Kick leapfrog time integration (Springel 2005):

$$\mathbf{v}^{n+\frac{1}{2}} = \mathbf{v}^n + \frac{\Delta t}{2} \mathbf{f}^n \quad (22)$$

$$\mathbf{x}^{n+1} = \mathbf{x}^n + \Delta t \mathbf{v}^{n+\frac{1}{2}} \quad (23)$$

$$\mathbf{v}^{n+1} = \mathbf{v}^{n+\frac{1}{2}} + \frac{\Delta t}{2} \mathbf{f}^{n+1} \quad (24)$$

where \mathbf{x}^i , \mathbf{v}^i are the particle positions and velocities at time step i , and \mathbf{f}^i are the forces at those timesteps. For the Kick-Drift-Kick method, the Poisson equation is solved after the particle or Drift update - with the updated positions of the particles. This method is formally second order accurate, apart from being symplectic in nature (Springel 2005).

The Drift-Kick-Drift method (Springel 2005)

$$\mathbf{x}^{n+\frac{1}{2}} = \mathbf{x}^n + \frac{\Delta t}{2} \mathbf{v}^n \quad (25)$$

$$\mathbf{v}^{n+1} = \mathbf{v}^n + \Delta t \mathbf{f}^{n+\frac{1}{2}} \quad (26)$$

$$\mathbf{x}^{n+1} = \mathbf{x}^{n+\frac{1}{2}} + \frac{\Delta t}{2} \mathbf{v}^{n+1} \quad (27)$$

is also second order accurate and symplectic, but we use the Kick-Drift-Kick method because the latter uses

the forces (and hence the potential) at full time steps, whereas the former uses the potential at half time steps. The test particles are going to be coupled to a fluid, whose own time integration scheme gives the potential at full time steps, and so using Kick-Drift-Kick is essential for the fluid and the particles to remain coupled to each other.

4.2. Hydrodynamics

As we saw earlier, we will be solving the continuity and Euler equations at early times when the smoothing length defined by Eq. (19) is larger than a grid cell, and most structure in the box is linear. At late times, when the smoothing length falls below a grid cell and highly non-linear structures start forming in the box, we will be solving only the continuity equation. Both equations are hyperbolic partial differential equations with source terms.

We use an operator splitting method to split any source term present in the equations from the hyperbolic advection part. We also use directional splitting (Toro 2009) so that the advection in 3 dimensions is reduced to 3 1-dimensional advectons. To solve the 1-dimensional advection problem on the grid, we employ a finite-volume scheme which is piecewise linear, and hence second order accurate in space.

The advection equation

$$\frac{\partial q}{\partial t} = -\frac{\partial(q u)}{\partial x} \quad (28)$$

is discretized so that the update equation for q_i^n , the value of q at cell center i at timestep n can be written as

$$\frac{q_i^{n+1} - q_i^n}{\Delta t} = -\frac{f_{i+\frac{1}{2}}^{n+\frac{1}{2}} - f_{i-\frac{1}{2}}^{n+\frac{1}{2}}}{\Delta x} \quad (29)$$

where $f_{i\pm\frac{1}{2}}^{n+\frac{1}{2}}$ are the fluxes at the cell edges at timestep $n+\frac{1}{2}$ constructed from the data at timestep n . The fluxes are constructed in the following manner:

$$f_{i+\frac{1}{2}}^{n+\frac{1}{2}} = 0.5 u_{i+\frac{1}{2}}^n \left((1 + \theta_{i+\frac{1}{2}}) q_i^n + (1 - \theta_{i+\frac{1}{2}}) q_{i+1}^n \right) + 0.5 |u_{i+\frac{1}{2}}^n| \left(1 - |c_{i+\frac{1}{2}}| \right) \phi(r_{i+\frac{1}{2}}^n) (q_{i+1}^n - q_i^n) \quad (30)$$

$$f_{i-\frac{1}{2}}^{n+\frac{1}{2}} = 0.5 u_{i-\frac{1}{2}}^n \left((1 + \theta_{i-\frac{1}{2}}) q_{i-1}^n + (1 - \theta_{i-\frac{1}{2}}) q_i^n \right) + 0.5 |u_{i-\frac{1}{2}}^n| \left(1 - |c_{i-\frac{1}{2}}| \right) \phi(r_{i-\frac{1}{2}}^n) (q_i^n - q_{i-1}^n) \quad (31)$$

where $c_i = u_i \Delta t / \Delta x$. We define $\theta_{i\pm\frac{1}{2}} = 1$ for $u_{i\pm\frac{1}{2}} > 0$ and $\theta_{i\pm\frac{1}{2}} = -1$ for $u_{i\pm\frac{1}{2}} < 0$. We further define

$$r_{i-\frac{1}{2}}^n = \begin{cases} \frac{q_{i-1}^n - q_{i-2}^n}{q_i^n - q_{i-1}^n} & \text{if } u_{i-\frac{1}{2}} > 0 \\ \frac{q_{i+1}^n - q_i^n}{q_i^n - q_{i-1}^n} & \text{if } u_{i-\frac{1}{2}} < 0 \end{cases} \quad (32)$$

and similarly for $r_{i+\frac{1}{2}}^n$. $\phi(r)$ is the flux limiter function which is required so that the method is Total Variation Diminishing (Harten 1983), by converting to a first order method near extrema in the profile of q . Even though there are no real shocks in the collisionless fluids that

we will be dealing with, once non-linear structures start forming in the box, there are sharp density gradients, which lead to spurious oscillations if the hydro scheme we use is not TVD in nature. Though the TVD property is essential for the stability of the code, it also means that there will be artificial diffusion near the extrema - sharper the change in gradient, larger the diffusion. In our code tests and cosmological simulations we use the Superbee flux limiter (Roe 1986), defined as

$$\phi(r) = \begin{cases} 0 & \text{if } r < 0 \\ \min(2r, 1) & \text{if } 0 < r < 1 \\ \min(2, r) & \text{if } 1 < r \end{cases} \quad (33)$$

This turns out to be the least diffusive flux limiter among the ones we tested.

While the piecewise linear method is formally correct to second order in time in smooth regions, it switches to first order time accuracy near saddle points and extrema. In cosmological simulations, especially the ones involving WDM, saddle points appear throughout the box as structures form and move under the influence of gravity. This means that, typically, the solution will only be first order accurate in large parts of the box. To make the scheme at least second order accurate in time throughout the box, we use a second order explicit Runge-Kutta time integration scheme. We use data at timestep n for the predictor step to get the predicted data at time $n + 1$, and then use this information in the corrector step to get the final solution at time $n + 1$. As we mentioned in the previous subsection, we calculate fluid quantities like the density at every full timestep, and therefore, to keep the particles and the fluid coupled, we use the Kick-Drift-Kick method which requires forces and potentials at every full time step, rather than the Drift-Kick-Drift method.

4.3. Gravity

We use Fast Fourier Transforms (FFT) to determine the potential on the grid from the densities of the neutrino fluid and WDM or CDM particles, just as in PM simulations (Hockney & Eastwood 1988). For CDM, we use cloud-in-cell (CIC) interpolation to obtain the grid density from the positions of the particles. In Fourier space, the Poisson equation is given by

$$\tilde{\phi}(\mathbf{k}) = G(\mathbf{k})\tilde{\delta}(\mathbf{k}) \quad (34)$$

where $G(\mathbf{k})$ is the Green function for the Poisson equation. On the grid, the discrete version of $G(\mathbf{k})$ becomes

$$G(k_x, k_y, k_z) = -C \left[\sin^2 \left(\frac{k_x}{2} \right) + \sin^2 \left(\frac{k_y}{2} \right) + \sin^2 \left(\frac{k_z}{2} \right) \right]^{-1} \quad (35)$$

where C is a constant independent of scale and $\{k_x, k_y, k_z\}$ are the wavenumbers on the cubic grid. Once we solve the Poisson equation using the FFT method, we

calculate forces on the grid using a four point stencil

$$f_x(i, j, k) = -\frac{\partial \phi_{(i,j,k)}}{\partial x} = -\frac{1}{12\Delta x} \left[8\phi_{(i+1,j,k)} - 8\phi_{(i-1,j,k)} - \phi_{(i+2,j,k)} + \phi_{(i-2,j,k)} \right] \quad (36)$$

where i, j and k label the coordinates of the grid points. These forces are then used to update the fluid when we solve the Euler equation. For updating the velocities of the particles, we again use a CIC interpolation to interpolate the forces from the grid to the positions of individual particles.

5. CODE TESTS

In this section, we present various tests of the new method described above. The first two tests are designed to check the accuracy of this method for the dynamics of virialized objects. The third test is devised to check accuracy at early times, when traditional N-body simulations can produce large errors. We then compare the results of this method to N-body results for a Λ CDM universe, where we know the latter yields accurate results. In our final test, we run simulations of Warm Dark Matter (WDM) cosmologies to check whether this method is able to eliminate the spurious halos that are known to plague both ‘‘hot start’’ and ‘‘cold start’’ N-body simulations of WDM cosmologies.

5.1. Plummer sphere advection

The Plummer sphere has an isotropic mass distribution with a radial density profile given by

$$\rho(r) = \left(\frac{3M}{4\pi b^3} \right) \left(1 + \frac{r^2}{b^2} \right)^{-5/2} \quad (37)$$

where b is the Plummer radius, which sets the size of the virialized region. The potential for the Plummer sphere is

$$\Phi(r) = -\frac{GM}{(r^2 + b^2)^{1/2}} \quad (38)$$

For this density profile, the phase space distribution function $f(\mathbf{r}, \mathbf{v})$ is (Binney & Tremaine 2011)

$$f(\mathbf{r}, \mathbf{v}) d\mathbf{r} d\mathbf{v} \propto (-E(r, v))^{7/2} r^2 v^2 dr dv \quad (39)$$

where $E = \Phi(r) + \frac{1}{2}mv^2$. At a given radius r , the probability of finding a particle with absolute velocity v is given by

$$\tilde{f}(v) dv \propto (-E(r, v))^{7/2} v^2 dv = \left(-\Phi(r) - \frac{1}{2}mv^2 \right) v^2 dv \quad (40)$$

Since the potential is known analytically at all values of r , the velocity distribution is known everywhere.

In our tests, we generate particles with density profile following (37) for $b = 5$ in grid units. For every particle we generate a random velocity whose magnitude is drawn from the probability distribution (40), and whose direction is drawn isotropically. To test advection, we give each particle an additional constant velocity. This

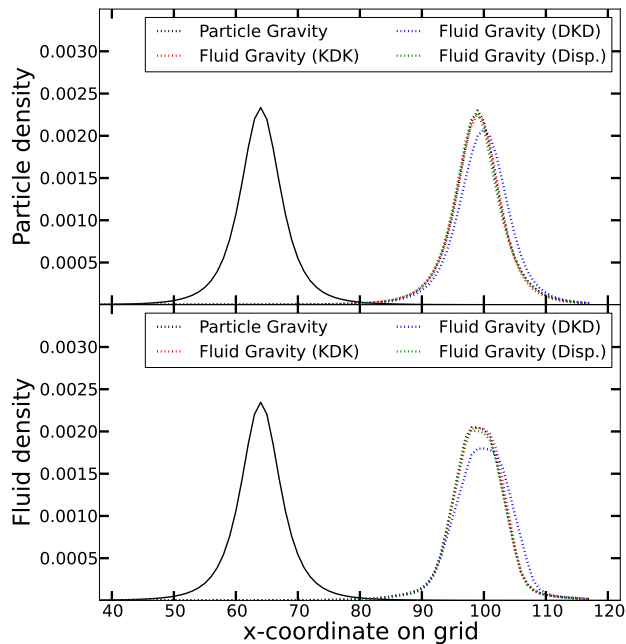


FIG. 1.— Density profile of an isolated advecting Plummer sphere with $b = 5$. The solid black lines indicate the initial density profile of particles (top panel) and fluid (bottom panel). The dotted lines in the top panel shows the final density profile of particles from 4 runs - a run where particles source gravity (black), a run where the fluid sources gravity and the particles are evolved using the Kick-Drift-Kick method (red), a fluid-sourced gravity run where the particles are evolved using the Drift-Kick-Drift method (blue), and a fluid-sourced gravity run where we estimated the velocity dispersion instead of the bulk velocity (green) - after 20 dynamical times. The dotted lines in the bottom panel shows the fluid profile from the same four runs after 20 dynamical times. While the other methods all agree well with the run in which particles source gravity, the Drift-Kick-Drift method is not suitable for coupling with our hydro scheme.

constant velocity will have the effect of shifting the Plummer sphere in space maintaining the shape of the density profile. We also initialize the fluid on the grid with the same density profile.

We evolve the particles and the fluid using the methods mentioned in §4. In our tests, we compare two different types of runs. In the first case, gravity is sourced by the particles, and so the fluid density acts as a tracer, evolving passively due to the motion of the particles. This provides a good check for our method - by comparing the particle and fluid density profiles at different times, we can see if the two descriptions of the same underlying dynamics do remain closely coupled to each other.

In the second type of runs, we use the fluid itself to source the gravity, which is the method we will use in our actual cosmological simulations. In this case, the particles act as tracer particles which are used only to estimate either the bulk velocity or the velocity dispersion on the grid. Again we check if the two density profiles - one from the particles and the other from the fluid - match each other at different times.

We compare these runs in Fig 1. We represent the particle-based gravity run by the black dotted lines. A fluid gravity run based on estimating bulk velocity from particles, and using Kick-Drift-Kick to update the particles is shown with the red dotted line. A similar run, but using Drift-Kick-Drift for the particles is plotted with

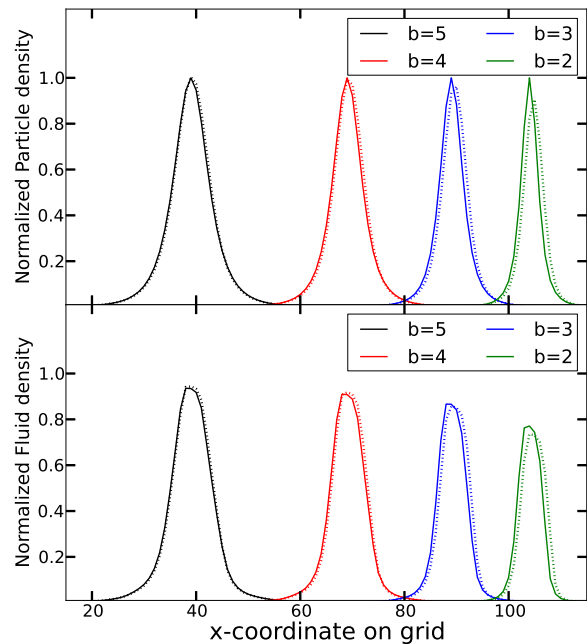


FIG. 2.— Density profiles for advecting Plummer spheres after 20 dynamical times for $b = 5$ (black), $b = 4$ (red), $b = 3$ (blue) and $b = 2$ (green). The solid lines represent the profiles from runs where gravity is sourced by particles. The dotted lines are from runs where the fluid sources gravity. The top panel plots the particle density profile, normalized by the maximum value of particle density for a given value of b from the particle based runs. The bottom panel plots the fluid density profiles with the same normalization. The profiles have been staggered for clarity.

the blue dotted line. Finally a fluid gravity run which the test particles (KDK evolution) to estimate the velocity dispersion is shown with the green dotted line. We see that the Kick-Drift-Kick method provides a better coupling to our hydro method than the Drift-Kick-Drift method. We also find that the run which used bulk velocity estimation and the run which used bulk velocity estimation agree very well. Therefore, whenever we do not need to smooth quantities to suppress shot noise, we will use the faster bulk velocity estimation method.

We next investigate how the results from these tests are affected by the resolution of the advecting Plummer sphere. In the previous example with $b = 5$, the Plummer sphere was resolved by roughly ten grid elements in each dimension, meaning it was well resolved. In cosmological simulations, depending upon the shape of the power spectrum, small virialized objects which are not well resolved may form. Therefore, we redo our test for $b = 4$, $b = 3$, and $b = 2$. We see from Fig. 2 that as we reduce the value of b , and therefore the resolution, the density profiles from the particle gravity runs after 20 dynamical times start to diverge from the fluid gravity runs. For the case where $b = 2$, the difference in the density profile of particles between the two types of runs (where particles source gravity and where fluid sources gravity) is as much as 15%. These differences grow over time, and will cause artificial damping of small scale structures.

We also test how the number of particles we use to estimate the bulk velocity or velocity dispersion on the grid affects the advection. We find that for $b = 5$, the results do not change much as long as we use more than $\sim 10^5$ particles as seen in Fig. 3.

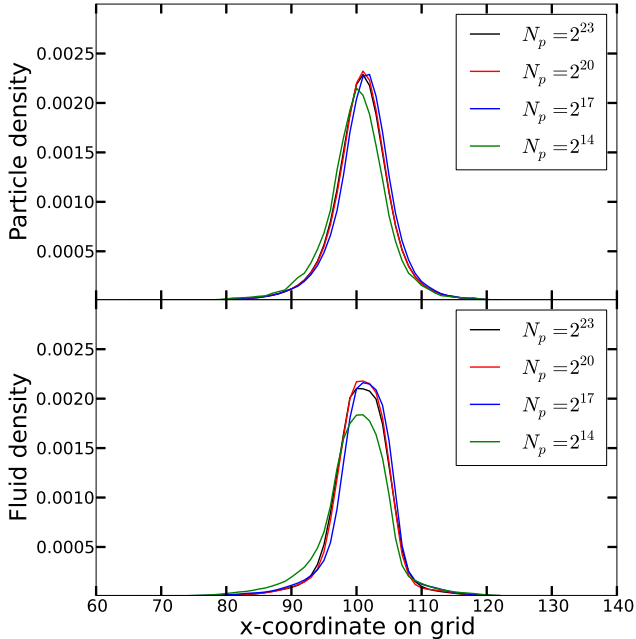


FIG. 3.— Particle (top panel) and fluid (bottom panel) density profiles for an advecting Plummer sphere with $b = 5$, with different number of test particles (N_p) used to sample the initial velocity distribution and estimate bulk velocity. We find that for this size, $N_p \sim 10^5$ is sufficient to follow the dynamics correctly.

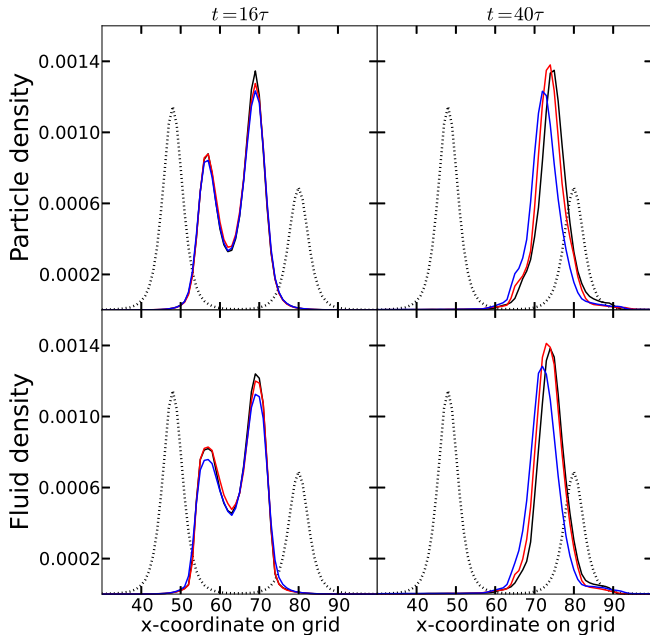


FIG. 4.— Evolution of the density profiles of two colliding Plummer spheres. The solid curves represent the particle density (upper panels) and fluid density (lower panels) for three different runs - gravity from particles (black), gravity from fluid Superbee (SB) flux limiter (red), and another fluid gravity run with Monotonized Central (MC) flux limiter (blue). The dotted curve in each panel shows the initial configuration. The left panels represent the densities when the Plummer spheres have passed through each other once. The right panels represent densities when the two spheres have merged.

5.2. Collision of Plummer spheres

To further test our code for dynamics of virialized objects, we next consider what happens when two individual Plummer spheres are made to advect through each other. If the two Plummer spheres form an isolated system, the mutual gravitational attraction would mean that the Plummer spheres would slosh through each other before finally merging into one bound object. The dynamics of this system is analogous to the ubiquitous merger of structures one finds in typical cosmological simulations.

In our test, we have two Plummer spheres with the same Plummer radius ($b = 5$ in grid units) but different masses. We use the same initialization technique as in the previous test - modified to take into account the different masses of the two spheres. We also give bulk velocities to the two Plummer spheres so that they move toward each other head on.

Once again, we compare what happens when gravity is sourced by the particles and when it is sourced by the fluid. For the latter case, we also compare how the results of this test is affected by our choice of the flux limiter for our hydro scheme. We show the comparison in Fig.4. We see that the particle profiles (top panels) and fluid profiles (bottom panels) of the run with the Superbee (SB) flux limiter (red curve) remain closer to the particle based run (black curve), than the run in which we used the Monotonized Central (MC) flux limiter (Van Leer 1977) (blue curves), especially at late times. This is understandable because the MC flux limiter is known to be more diffusive than the Superbee.

5.3. Linear growth rate

In cosmology, the high-redshift growth of the power spectrum of all species, including light particles like neutrinos and heavy particles like WDM, can be calculated in linear theory. We use the linear Boltzmann code CLASS (Lesgourgues 2011; Blas et al. 2011; Lesgourgues & Tram 2011) to do these calculations. The power spectrum and transfer functions from CLASS at the starting redshift, z_{start} , are used to initialize our simulations. The evolution of the power spectrum from the simulation boxes can then be compared at later redshifts to the outputs from CLASS at those redshifts.

In simulations involving light neutrinos, linear perturbation theory can be used to describe the evolution of the neutrino power spectrum for most of the evolution, except maybe at very late times. This means that for most of the simulation, the smoothing length defined in Eqn. (19) is larger than a pixel, and we need to estimate the velocity dispersion from the test particles. Comparing the growth of the power spectrum at these times against CLASS provides a test for the code when it is solving both Eqns. (7) and (11). Note that at these early times, the growth of the neutrino power spectrum is scale dependent. On scales larger than the free streaming scale of the neutrinos, the neutrino power spectrum grows at the same rate as the CDM power spectrum. Below the free streaming scale, however, different scales can grow at different rates. To compute the growth factor accurately on all scales, it is essential to determine the correct “effective sound speed” for the neutrinos. This is exactly what we estimate from the velocity dispersion. The effective sound speed depends on redshift, meaning that a comparison of the power spectrum at different times

provides a test for the accuracy of our estimates of the velocity dispersion. In Fig. 5, we show the growth of the neutrino power spectrum for a neutrino species of mass $m_\nu = 0.1$ eV at redshifts $z = 22.53$ and $z = 0$. We compare the results from our simulations to the growth predicted by CLASS for the same cosmology. We see that the power spectra from our simulations match the linear theory predictions quite well at all scales in the simulation box at $z = 22.53$. Leaving aside the large scales, which are affected by sample variance, there are, however, differences of about 10% even on the smaller scales. This arises from the fact we use the particles directly to get the velocity dispersion, while in CLASS, an approximation is used to evaluate the sound speed when the fluid approximation is turned on (Lesgourgues & Tram 2011). We have checked that if we use the same approximation in our code, instead of the stress tensor from the particles, we match the CLASS results to within a few percent. However, this small difference in the neutrino power spectrum will have minimal effect on the observable matter power spectrum. We note that all our comparisons with CLASS were with the fluid approximation turned on, which means that the effective sound speed of the neutrinos is treated to be scale independent. While this is done explicitly in CLASS when the fluid approximation is turned on, in our simulations, the large smoothing length at early times for light neutrino species means that the velocity dispersion is scale independent over much of the simulation box - effectively using the fluid approximation.

To illustrate the effect of shot noise in neutrino simulations, we also plot in Fig. 5 the neutrino power spectrum at the later redshifts. These spectra were obtained from a simulation which treats the neutrinos as N-body particles. The power spectrum of neutrinos from this simulation is dominated by shot noise for most scales in the box - this is true even at $z = 0$.

In Fig. 6, we show an example of a WDM simulation. In this case, while the power spectrum is initially damped at small scales, non-linear structure does develop at high k as time progresses. The power spectrum on these scales will then disagree with the linear CLASS power spectrum. However, if the simulation volume is large enough, then the largest scales in the box will still be well described by linear theory, and can be matched to the outputs from CLASS. Unlike the neutrino simulations, where the energy density and gravitational potential are dominated by CDM particles, the growth of the matter power spectrum in the WDM simulations is governed by the fluid, and testing the growth rate in these simulations provides a stronger test of the coupling between the fluid equations and the gravitational potential. Fig. 6 shows the growth of the power spectrum from a 200eV WDM particle compared to the outputs of CLASS at two different redshifts, $z = 60.54$ and $z = 27.57$. At these early times, our method is able to reproduce the linear results down to almost the smallest scales in the box.

5.4. CDM comparison run

Even though our method is meant to be used in cosmologies which include particles whose thermal velocities cannot be ignored, we can test the validity of our method by using it for a standard CDM cosmology run,

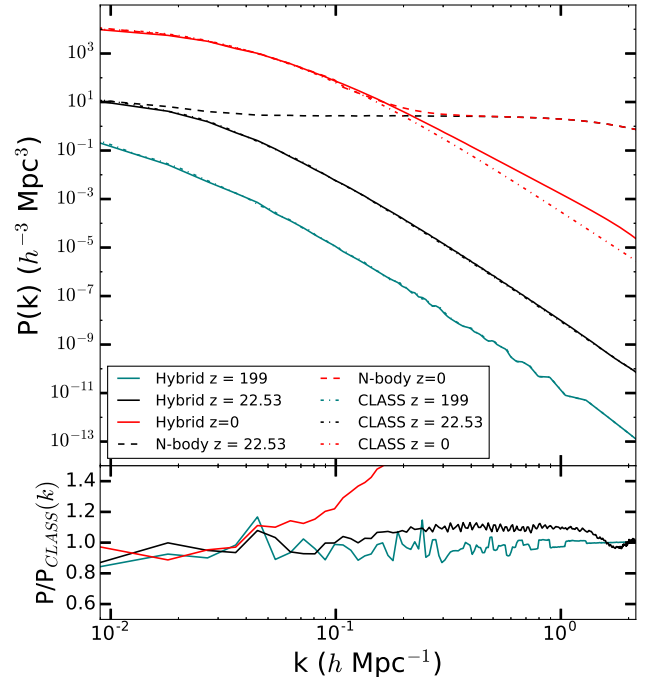


FIG. 5.— Comparison of the growth of the power spectrum of neutrinos ($m_\nu = 0.1$ eV). The top panel plots the comparison of the power spectra from the hybrid simulations (solid lines) to the outputs from CLASS (dot-dashed lines). We plot the initial power spectra at $z = 199$, as well as at redshifts of $z = 22.53$ and $z = 0$. We also plot the power spectra (dashed lines) at the later redshifts from an N-body treatment of neutrinos, which are dominated by shot noise at small scales. In the bottom panel we plot the ratio of the power spectra from the hybrid simulations to the linear theory results at $z = 199$ (teal), $z = 23.53$ (black) and $z = 0$ (red).

and comparing the results to those of an N-body simulation. Since N-body simulations are known to be accurate for CDM-only cosmologies, this comparison allows us to test our method starting at high redshifts when linear theory is valid to late times and low redshifts where we can test the non-linear evolution of our method.

For this comparison, we do not need to smooth quantities, since there are no random particle velocities which will lead to thermal shot noise. We use the test particles to measure the bulk velocities on a grid at all redshifts, and use these velocities to solve the continuity equation (7) to evolve the densities forward. Both simulations are done on a $140 h^{-1} \text{Mpc}$ box with $\Omega_\Lambda = 0.7$ and $\Omega_{\text{CDM}} = 0.3$. The Hubble constant H_0 is taken to be 70 km/s/Mpc . Both sets of simulations used 512^3 particles with a 512^3 grid to calculate the gravitational potential. Our method also uses a 512^3 grid to store densities and bulk velocities. Initial conditions are generated at redshift $z = 99$ using CLASS.

We begin by comparing the growth of the power spectrum on scales which remain linear - the largest scales in the simulation box. At early times, the growth at these scales matches the growth from standard N-body simulations. This agreement persists even to times when halos start forming in the box. However, at very late times, the agreement breaks down, and the largest scales grow at a rate slower than in N-body simulations. This can be seen clearly from the lower panel in Fig. 7, where the ratio of the power spectrum from our hybrid simulation to

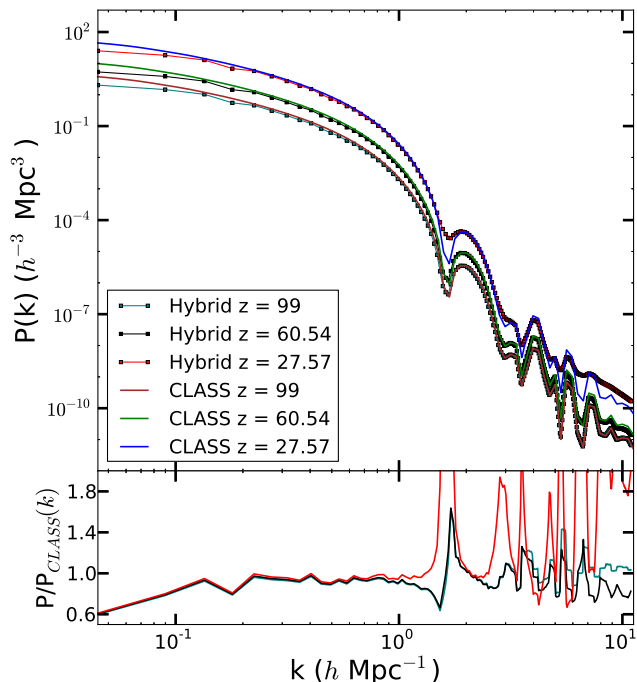


FIG. 6.— Linear growth of the power spectrum for a WDM particle of mass 200eV. The top panel plots the power spectrum at initial redshift $z = 99$ and at $z = 60.54$ and $z = 27.57$ from the hybrid simulations and from linear theory. The bottom panel plots the ratio of the power spectra from the simulations and from linear theory at $z = 99$ (teal), $z = 60.54$ (black) and $z = 27.57$ (red). At large scales in the box, the ratio is different from 1 due to sample variance.

the power spectrum from the N body calculation (both at $z = 0$) is less than 1 at even the largest scales in the box.

At late times in these CDM simulations, structures form at all scales and at all locations. Even deep inside voids, there are small fluctuations in the density field. Because of these small variations, the density field is not smooth over most of box, and there are large numbers of local extrema and saddle points along any of the axes of the simulation box. As mentioned in §4.2, our hydrodynamic scheme needs to switch over to a spatially first order scheme whenever it encounters a saddle point - unphysical oscillations set in when this condition is not satisfied. Due to the numerous saddle points which develop late in these CDM simulations, our method is forced to solve the governing equations of motion in a spatially first order manner over most of the pixels in the box. First order methods are known to be highly diffusive - even up to scales comparable to the entire simulation box. Because of this, the power at large scales is damped, and the growth rate of these scales becomes unphysically slow. We found that most of the pixels at which the hydrodynamic method is forced to go first order lie inside voids and regions where $|\delta| \sim 1$, rather than inside halos or regions where $|\delta| \gg 1$. Note that this problem is not as severe for WDM cosmologies in which the streaming scale is resolved. However, there is still numerical diffusion on small scales compared to an N-body treatment, and we will discuss below in §5.5 how this can be remedied using an SPH-like approach at early times.

To further illustrate the effects of artificial diffusion,

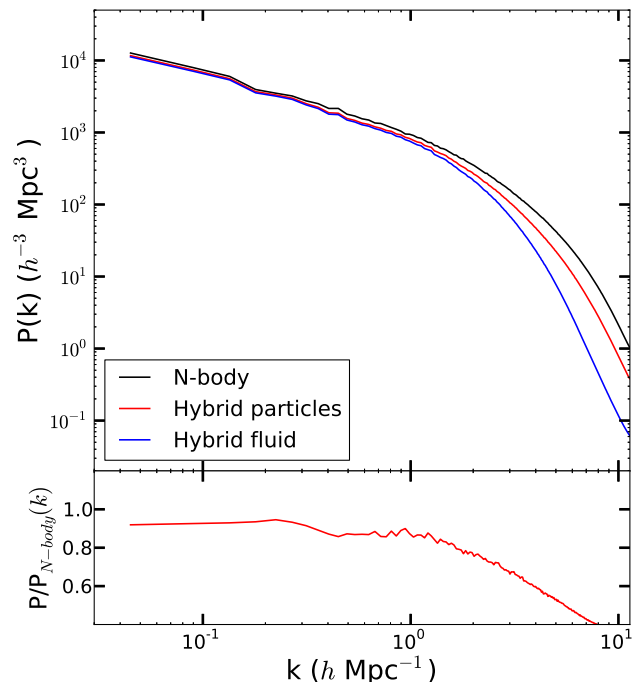


FIG. 7.— Final power spectrum at $z = 0$ for CDM runs. In the top panel, we plot the results a normal N-body run (black) as well as from the particles (red) and fluid (blue) in our hybrid simulations. In the bottom panel we plot the ratio of the particle power spectrum from the hybrid simulations to the power spectrum from the N-body run.

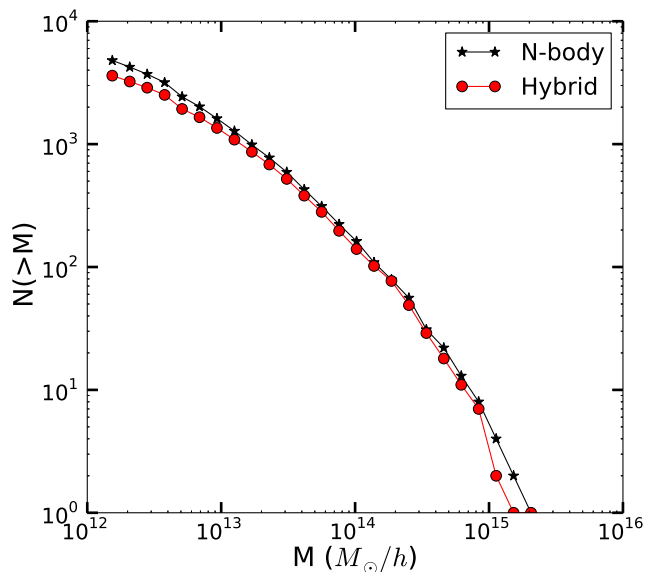


FIG. 8.— Mass function from the N-body run (black) and the hybrid Eulerian method (red) for a Λ CDM cosmology. The red curve shows a deficit of halos at all mass scales, including near the high end of the mass function. In contrast, the hybrid Lagrangian (SPH) method is formally identical to N-body for CDM cosmologies.

we next compare the mass functions of halos from our simulations to N-body halo mass functions. To find halos in our simulations, we use the Rockstar halo finder (Behroozi et al. 2012) as well as a spherical overdensity halo finder. For the latter method, we define a halo as spherical regions of radius R_{halo} around overdensity

peaks within which the average enclosed matter overdensity is greater than 200. The associated halo mass is then defined as

$$M_{\text{halo}} = \frac{4}{3}\pi R_{\text{halo}}^3 \times (200 \Omega_m \rho_{\text{crit}}) \quad (41)$$

where ρ_{crit} is the critical density of the universe.

In our simulations we can use either the fluid density or the test particle density to define halos. Since there is no thermal shot noise in the test particle density field in these CDM simulations, there is no problem using the test particle densities in our halo finder. However, we can also do the same even in WDM simulations where there is shot noise from the thermal velocities of particles. This is because throughout the simulation, we never use the test particle density to source gravity, hence the shot noise in the density field is not allowed to grow gravitationally. Therefore the shot noise fluctuations in the density field of the test particles arise at an early time and become frozen once the particles cool down. These initial fluctuations are much smaller than overdensities of $\delta \sim 200$ that are needed for a halo to be detected. Therefore, the halos that we detect at late times in the density field of test particles are real halos and not shot noise artifacts. This would not have been true if we had used the test particle density instead of the fluid density in the Poisson equation - in that case, the small shot noise fluctuations would have grown gravitationally over time and produced spurious halos.

Comparing mass functions, we find that if the halos defined using the test particle densities rather than fluid densities, the results match those from the N-body simulations more closely. This is expected from the tests we performed in §5.1 and §5.2 - the fluid profile near the center is flattened by artificial diffusion. The particle profile is not as affected on scales which are well-resolved on the grid. However, there are still differences between the mass functions from our simulations compared to the N-body mass functions. Also, there are differences on small scales between the N-body power spectrum and the power spectrum from our simulations. This is once again due to artificial diffusion on small scales. For small halos with steep profiles, the flattening of the fluid profile means a large fraction of the mass is moved away from the peak. This also ends up affecting the test particles which respond to the gravitational field of the fluid.

This loss of smaller scale power due to diffusion leads to fewer smaller halos found in our simulation box than in the corresponding N-body boxes. However, at a given redshift, this can also cause differences in the masses of large, fast-accreting halos. This is because the lack of small scale power alters the dynamics of the halos and also the time at which mergers happen - the mergers in our simulations lag behind the corresponding merger in the N-body simulation, as can be seen in Fig. 9. The fast accreting halos at a given redshift have a rapid change in their mass because of successive mergers. Because these mergers have not yet happened in the our simulations, the halos are at a lower mass. This shows up in the mass function as a lack of halos at the largest masses, as can be seen in Fig. 8.

Our findings show that in the CDM case, numerical diffusion in our grid-based fluid method affects all useful quantities measured from the simulation boxes - even

at the largest scales. This motivates us to use a more Lagrangian approach for simulations in which there is structure on all scales in the box. Specifically, we adopt the SPH-like approach that we outlined in §3.3 for WDM simulations where the fluid that we are simulating is the main source of the gravitational potential. As the results in this section have shown, for such simulations any numerical diffusion becomes important. In contrast, for neutrino simulations, where the gravitational potentials are highly dominated by the CDM, we will continue to use grid-based Eulerian methods, as our implementation of SPH is computationally more expensive than our implementation of grid-based hydrodynamics.

5.5. Simulating Warm Dark Matter cosmologies

In our final test, we simulate WDM cosmologies to see if our fluid methods can eliminate the artifacts generated for these cosmologies when simulated using N-body techniques. For N-body simulations which include the random thermal velocities of the WDM particles - or a hot start - these artifacts are spurious halos seeded by shot noise in the density field. For cold start simulations which do not include the thermal velocities, the artifacts are “beads on a string” halos studied extensively by Wang & White (2007).

For WDM, there is a characteristic free streaming scale below which the linear power spectrum is damped. Above this scale, the behavior of WDM is the same as CDM, so we will concentrate on simulations in which the free streaming scale is resolved. To estimate the scale of this damping, we take the linear power spectrum at $z = 0$ for CDM and the WDM particle we are interested in. We find the R_{damp} such that the CDM power spectrum convolved with $|W(kR_{\text{damp}})|^2$ gives the WDM power spectrum (Villaescusa-Navarro & Dalal 2011), where $W(kR)$ is the Fourier transform of the top-hat window function with radius R . We also define a damping mass scale

$$M_{\text{damp}} = \frac{4}{3}\pi R_{\text{damp}}^3 \Omega_m \rho_{\text{crit}} \quad (42)$$

where ρ_{crit} is the critical density of the universe.

For these WDM simulations, we use the hybrid SPH method laid out in Sec. 3.3 to suppress the effects of numerical diffusion. It is important to do so, because we are interested in determining the halo mass function below the damping scale down to the smallest scales in the box, and these scales are most affected by diffusion.

To validate our hybrid SPH method, we first run a simulation for a WDM particle with mass $m = 200$ eV, for which the damping scale is $3.3h^{-1}$ Mpc. We do three runs for this cosmology, a hot start N-body run, a cold start N-body run, and a run using our hybrid SPH method. The initial thermal velocities are included in both the hot start run and our SPH method. These simulations were done on 512^3 grids with 1024^3 particles, and for the background cosmology we used $\Omega_\Lambda = 0.7$, $\Omega_m = 0.3$ and $H_0 = 70$ km/s/Mpc. The size of the simulation volume was $(140h^{-1}\text{Mpc})^3$.

We first compare the final power spectra from all three simulations at $z = 0$, as illustrated in Fig. 10. We see that at large scales, the power spectra from all three runs agree with each other. However, at small scales, while the cold start N-body run and our hybrid SPH run give

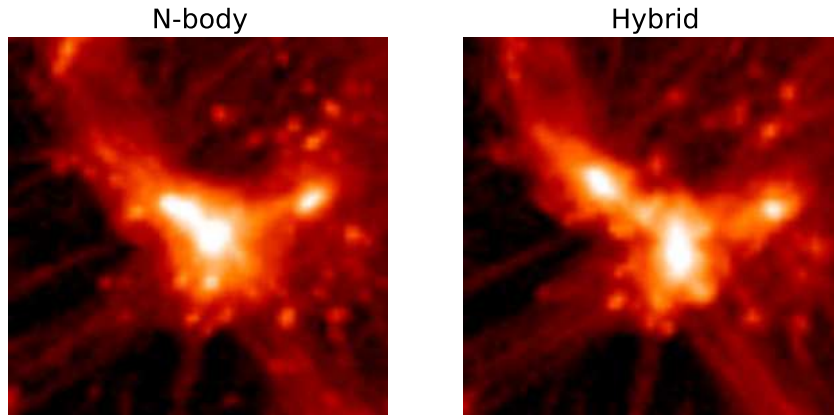


FIG. 9.— A zoom-in of a halo at $z = 0$ from the CDM comparison simulations - the left panel shows the density field from a standard N-body simulation, while the right panel shows the density field from our hybrid method. In the N-body case, the central object has already merged, whereas in the hybrid method, the two objects are still distinct.

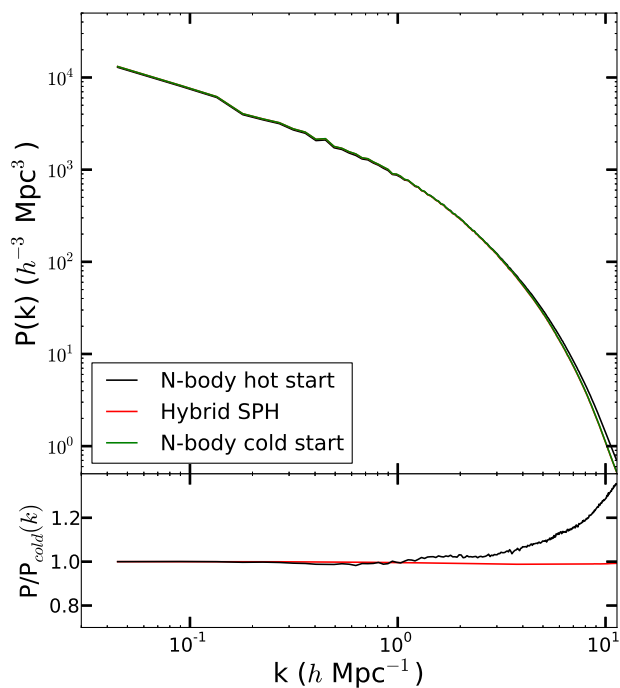


FIG. 10.— Final power spectrum at $z = 0$ for WDM species with mass 200 eV. In the top panel, we plot the results from a hot N-body run (black), a cold N-body run (green), as well as our hybrid SPH simulation (red). The results from the SPH run and the cold start N-body run are virtually indistinguishable. On large scales in the box, the hot start N-body run agrees with the other two, but there are differences on small scales. In the bottom panel we plot the ratio of the particle power spectrum from the hybrid SPH run to the cold N-body power spectrum (red) to show that these methods match each other down to the smallest scales resolved by this simulation box, even though the initial conditions of the SPH run was the same as that for the hot start N-body run. We also plot the ratio of the power spectra from the hot run to the cold run (black) to show their difference on scales affected by the streaming of particles.

the same results, the power spectrum from the hot run starts to deviate from the others. This is expected in the hot run as the shot noise due to random streaming of the simulation particles leads to the presence of ex-

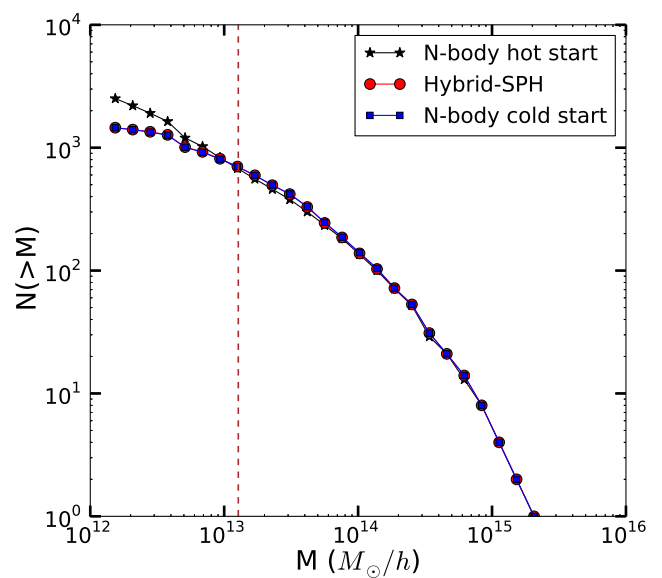


FIG. 11.— Mass function for WDM species with $m = 200$ eV. We plot results from a hot N-body run (black), a cold N-body run (blue), and our hybrid SPH method (red). The brown dashed line represents M_{damp} defined in Eqn. (42). The hot run shows the presence of many halos below M_{damp} , while the other runs do not show these smaller halos.

tra power at small scales, and this noise grows over the course of the simulation. However, we note that even though we included these thermal velocities in our hybrid SPH method, the final result agrees very well with that from the cold start run, down to the smallest scales that we resolve in this simulation box. This can be seen clearly from the bottom panel of Fig. 10, where we plot the ratio of the two power spectra, and find that the ratio is very close to 1 at all scales.

We also compare the halo mass functions from the three runs in Fig. 11. We expect the effect of the streaming length of the WDM particle to show up at masses below M_{damp} represented in the plot by the dashed brown line. Since the power spectrum was initially damped on these scales, we expect very few halos with these low masses to form in the box. That seems to agree with

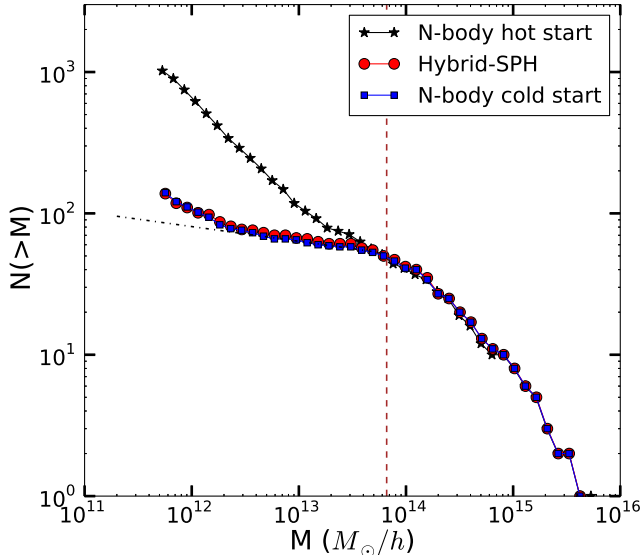


FIG. 12.— Mass function for WDM species with $m = 60\text{eV}$. We plot results from a hot N-body run (black), a cold N-body run (blue), and our hybrid SPH method (red). The brown dashed line represents M_{damp} . Below M_{damp} the hot run shows a number of spurious halos. At even smaller scales, both the cold start and the hybrid SPH run start showing “beads on a string” artifacts. The black dash-dotted line is an extrapolation from the flat part of the halo mass function.

what we see from both the cold start run and the hybrid SPH run - the cumulative mass function flattens off at mass scales smaller than M_{damp} . However, the hot run does show the presence of many small halos. These are the spurious halos which were seeded by the shot noise arising from the thermal motions at early times.

These results suggest that our hybrid SPH method is effective in eliminating the effects of shot noise. Even though we started off by taking into account the thermal velocities of the particles from the Fermi-Dirac distribution, our final results agree very well with simulations which do not include these thermal velocities, and are therefore immune to this form of shot noise.

However, as discussed earlier, the cold start simulations for WDM show “beads on a string” artifacts (Wang & White 2007), produced when structures collapse along grid lines in the simulations. We check if our method can be used to get rid of these artifacts, which once again shows up in the mass functions at scales much smaller than the damping scale. For this, we simulate a lighter WDM particle, $M = 60\text{eV}$, for which $R_{\text{damp}} \sim 10.2 h^{-1}\text{Mpc}$. This allows us to resolve scales much smaller than the streaming scale in our simulation box. We choose our background cosmology similar to that used in Wang & White (2007): $\Omega_m = 1$, $H_0 = 70\text{ km/s/Mpc}$ and $A_s = 4.6 \times 10^9$, where A_s is the amplitude of the primordial power spectrum. The size of the simulation volume was $(70h^{-1}\text{Mpc})^3$. As before, we run both hot start and cold start N-body runs to compare to our simulations.

We compare the mass function from the three runs in Fig. 12. Once again we see that the hot run produces many spurious halos below M_{damp} . In the cold run and the hybrid SPH run, we see that the cumulative mass function flattens just below the damping scale, meaning

that very few halos are produced in this mass range. At scales much smaller than the damping scale, the cold start run shows an up-turn in the mass function. This upturn is due to the halos collapsing along grid lines in simulations because of very low power on small scales. The black dash-dotted line is an extrapolation of the flat part of the mass function to show how these “beads on a string” halos affect the mass function. We see the same feature even in the hybrid SPH run, where the mass function follows that from the cold start N-body closely down to the scales where the artificial halos start showing up.

From this test we conclude that while our hybrid method is highly effective in eliminating shot noise in WDM simulations where the initial thermal velocities of particles are taken into account, they cannot get rid of the “beads on a string” artifacts seen in cold start N-body simulations of WDM cosmologies. Since this hybrid method is computationally much more expensive than N-body methods, and since applying our method to WDM simulations yields no advantage over the traditional cold-start N-body simulations, we do not find a persuasive reason to use this in further studies of WDM cosmologies.

6. NEUTRINO SIMULATIONS

In this section, we discuss examples where our simulations are applied to cosmologies containing massive neutrino species. We will mostly focus on relatively low-resolution simulations of large volumes that contain a large fraction of the neutrino free streaming scale; in future work we will study nonlinear structure formation with neutrinos at higher resolution. Because of the low spatial resolution, most halos will be unresolved. However, cosmic voids can be studied using these simulations, and as we show below, massive neutrinos can have interesting effects on the large-scale clustering of highly empty voids. Indeed, from simple physical arguments we can expect that neutrinos will have a more significant impact on voids than on halos. While some neutrinos, mostly coming from the low momentum tail of the initial distribution function, do get captured by massive halos at late times, the average enclosed overdensity Δ_ν of neutrinos is still much smaller than the average enclosed overdensity of CDM, $\Delta_{\text{CDM}} \sim 200$. Any effects from neutrinos would be expected to be of the order of $f_\nu \Delta_\nu / (f_{\text{CDM}} \Delta_{\text{CDM}}) \lesssim 1\%$. This effect has been verified already (Villaescusa-Navarro et al. 2014; LoVerde 2014, 2016). Inside deep voids, on the other hand, the CDM overdensities are ~ -1 , while the neutrino overdensities are not as negative due to their thermal dispersion. This means that the overall mass of the neutrinos in the void can be comparable to the total mass of CDM. Therefore we might expect any effects due to neutrinos to be magnified for voids, compared to halos. Note that throughout this section, we define voids using a threshold on the total matter density, including both CDM and neutrinos. This is in contrast to voids defined using only the CDM densities, as used by Massara et al. (2015) to study the profiles of voids in the presence of neutrinos.

Since our purpose here is to demonstrate and highlight certain effects, for the void studies, we will use parameters which help best illustrate these. Our simulations use a box whose size is $700h^{-1}\text{Mpc}$ with $\Omega_\Lambda = 0.7$ and $\Omega_{\text{CDM}} = 0.27$, along with a single neutrino species of

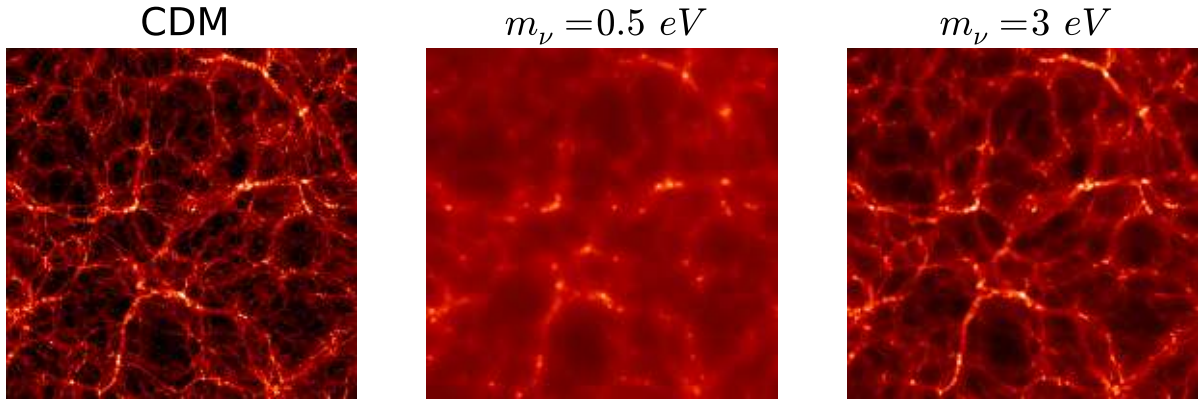


FIG. 13.— A slice through the density field in the simulation boxes at $z = 0$ for two neutrino masses - 0.5 eV and 3 eV. The simulation box side length is $175 h^{-1}$ Mpc. The left panel shows the CDM density field, the middle panel shows the density field for the 0.5 eV neutrino, while the right panel shows the density field for the 3 eV neutrino. For the lighter neutrino, on large scales, the density traces the underlying cosmic web structure laid down by the CDM component, but is much more diffuse on small scales. For the heavier neutrino, the density field is less diffuse and follows the CDM density more closely down to smaller scales.

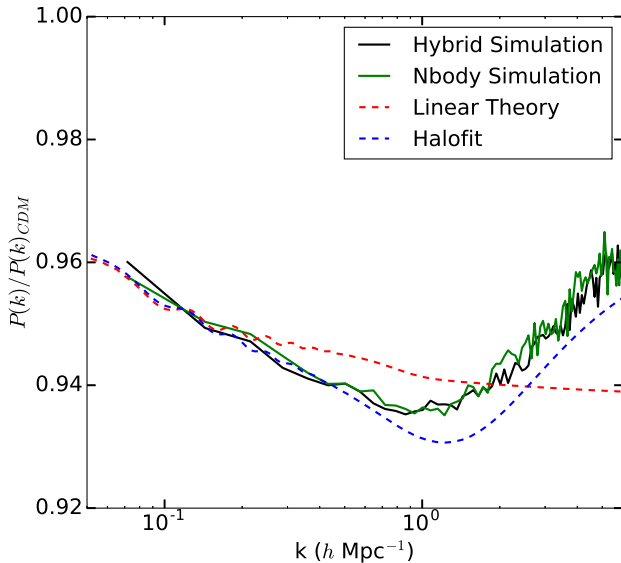


FIG. 14.— Relative damping of the matter power spectrum in the presence of a massive neutrino with $m = 0.1$ eV with realistic energy density ($\Omega_\nu \approx 0.0022$), compared to the CDM-only prediction. The linear theory prediction is plotted with the dashed red while the dotted blue curve represents the HALOFIT prediction. The solid black curve is the result of our hybrid simulation, while the solid green curve is from a simulation treating neutrinos as another set of N-body particles.

mass $m_\nu = 0.1$ eV. Neutrinos of this mass would give energy density $\Omega_\nu < 10^{-3}$, producing relatively subtle effects on nonlinear structure formation. To amplify neutrino effects in our simulations, we therefore use an unphysically large number density, to give $\Omega_\nu = 0.03$. We stress that this is only for illustrative purposes; later on we will show results for realistic energy densities. For this Ω_ν , we have

$$f_\nu = \frac{\Omega_\nu}{\Omega_{\text{CDM}} + \Omega_\nu} = 0.1. \quad (43)$$

The Hubble constant H_0 is taken to be 70 km/sec/Mpc. We use 512^3 CDM particles and 1024^3 neutrino test particles with a 512^3 grid for hydrodynamic quantities. Initial conditions for both species are generated using CLASS at redshift $z = 49$.

Non-linear structures like voids are known to be biased tracers of the underlying matter field. The overdensity in the void field is denoted by δ_{void} . If the universe contains only one species, say CDM, we can write

$$\delta_{\text{void}}(k) = b(k)\delta_{\text{CDM}}(k) \quad (44)$$

where $b(k)$ is the scale-dependent bias factor. On large linear scales, $b(k)$ is independent of k for these CDM only simulations (Scherrer & Weinberg 1998). Using Eqn. (44), this linear (large-scale) bias factor is given by

$$b = \frac{P_{\text{void,CDM}}(k)}{P_{\text{CDM}}(k)} \quad (45)$$

where $P_{\text{void,CDM}}(k) = \langle \delta_{\text{void}}^*(k)\delta_{\text{CDM}}(k) \rangle$ is the cross spectrum between the void overdensity field and the underlying CDM overdensity field and $P_{\text{CDM}}(k)$ is the CDM auto-power spectrum.

If a new species is added to the matter content of the universe, biasing is no longer as simple. In this case, the void overdensity depends on both the CDM and neutrino overdensities, δ_{CDM} and δ_ν . Eqn. (44) should then be replaced by

$$\delta_{\text{void}}(k) = b_{\text{CDM}}(k)\delta_{\text{CDM}}(k) + b_\nu(k)\delta_\nu(k) \quad (46)$$

In terms of the total underlying matter field

$$\delta_{\text{tot}} = f_{\text{CDM}}\delta_{\text{CDM}} + f_\nu\delta_\nu \quad (47)$$

we can write

$$\delta_{\text{void}}(k) = b_{\text{tot}}(k)\delta_{\text{tot}}(k) \quad (48)$$

Even on large scales where the perturbations are linear, the neutrino power spectrum and the CDM power spectrum can be different from one another, implying that $b_{\text{tot}}(k)$ will not be scale independent. This scale dependent bias in large-scale structure can be an extremely powerful signature because it does not arise in standard cosmologies. Producing scale dependent bias on linear scales generally requires violating locality of the formation of biased tracers, for example due to non-gaussianity (Dalal et al. 2008) or large scale modifications to gravity (Jain & Khoury 2010).

In the case of massive neutrinos, the scale dependence of $b_{\text{tot}}(k)$ depends on the difference of the two power

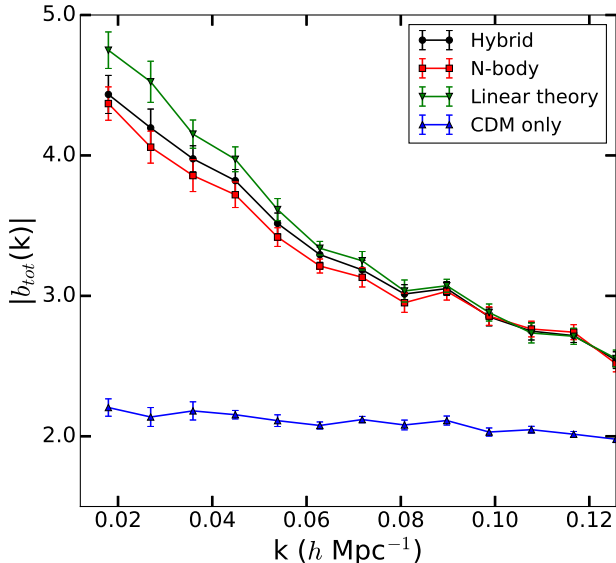


FIG. 15.— Absolute value of the bias defined in Eq. (48) as a function of scale, averaged from 8 runs for $m_\nu = 0.1 \text{ eV}$ and $f_\nu = 0.1$. The voids were defined using the underdensity in the total matter field. The threshold for void definition was set at -0.7 . We compare the results from our simulations (black) to the other existing methods of treating the neutrinos as a linear fluid (green) and treating neutrinos as a set of particles with a different mass in N-body simulations (red). Our method and the N-body method yield results which match to within error bars, but show a strong scale dependence. The linear method shows an even stronger scale dependence. We also plot (in blue) the bias for voids defined in exactly the same manner from 8 CDM-only runs in for which the final power spectrum matches the final CDM power spectrum for the runs including neutrinos.

spectra as a function of scale, and hence the mass of the neutrino species. For heavier neutrinos, the free streaming scale may lie well inside the simulation box. We know that on scales well above the free streaming scale, perturbations to both neutrinos and CDM evolve similarly, and so their power spectra on large scales will be identical at late times. In this case $b_{\text{tot}}(k)$ will indeed be scale independent. However for lighter neutrinos with very long free streaming lengths, the power spectra at linear scales will be very different for the neutrinos, compared to CDM. In this case, $b_{\text{tot}}(k)$ can be strongly scale dependent.

In our simulations we define the total matter overdensity as in Eqn. (47) and then use spherical overdensity void finder. We define voids as those regions around a density minimum in which the averaged overdensity is below the cutoff of -0.7 . We then select the largest voids in the box, so that we are not affected by exclusion effects. We run 8 sets of simulations with different realizations of the power spectrum. We calculate the linear bias in each of these 8 realizations, and then average over them to reduce the sample variance.

Plotting the bias defined in Eqn. (48) in Fig. 15, we find that it is indeed strongly scale dependent. To make sure that this scale dependent linear bias is not an artifact of our simulation method, we perform simulations of the same cosmology using two other methods. In one, we treat the neutrinos as an additional species with a different mass in an N-body code. In the other, we treat the neutrino fluid in a linear approximation scheme. We

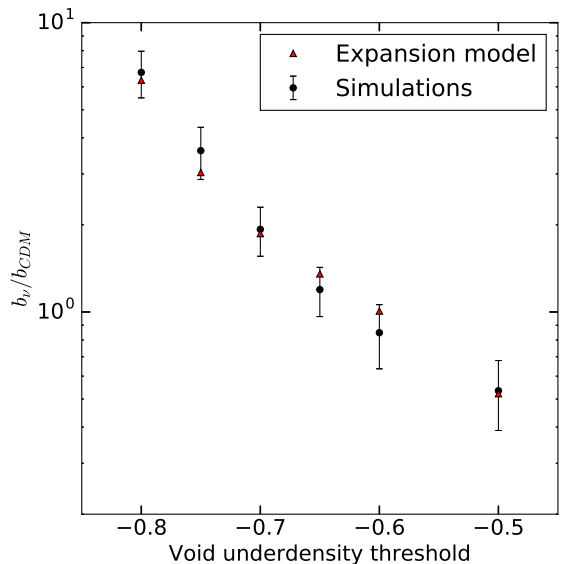


FIG. 16.— Comparison of the ratio of Eulerian biases b_ν and b_{CDM} at $f_\nu = 0.1$, defined in Eqn. (46), measured in simulations (black circles) vs. predictions from the spherical expansion model (red triangles), as a function of the threshold floor used in the void definition. The bias ratio diminishes for decreasing void thresholds, a trend quantitatively predicted by the spherical expansion model. The error bars represent the errors on the best fit values from the simulations.

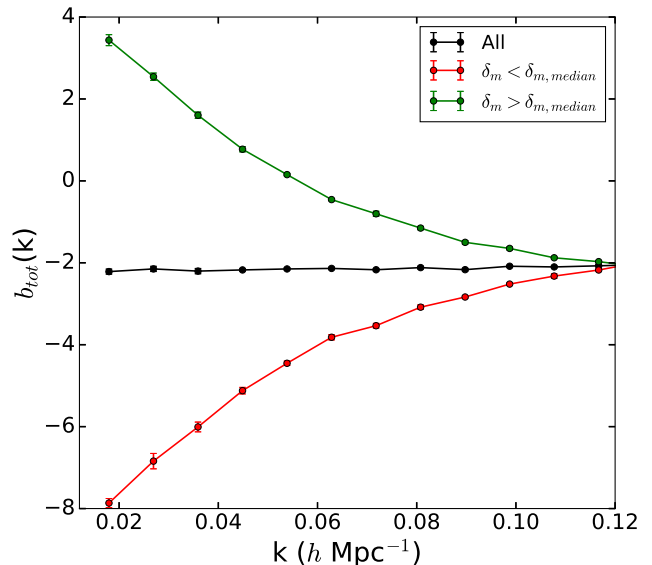


FIG. 17.— Behavior of the void bias from the hybrid simulations when the voids are selected using the CDM field only, and then split on the basis of the enclosed total matter overdensity for $m_\nu = 0.1 \text{ eV}$ and $f_\nu = 0.1$. The black curve represents $b_{\text{tot}}(k)$ for voids selected using the CDM field only with overdensity threshold of -0.7 . The red curve represents $b_{\text{tot}}(k)$ for the subsample of voids whose enclosed total matter overdensity was lower than the median enclosed total matter overdensity in the above sample. Similarly, the green curve shows $b_{\text{tot}}(k)$ for the subsample whose enclosed total matter overdensity is higher than the median.

then use the same criterion we have defined above to find voids and calculate the large scale bias. We find that the scale dependent bias we see in our method matches the result from the N-body method to within our error bars,

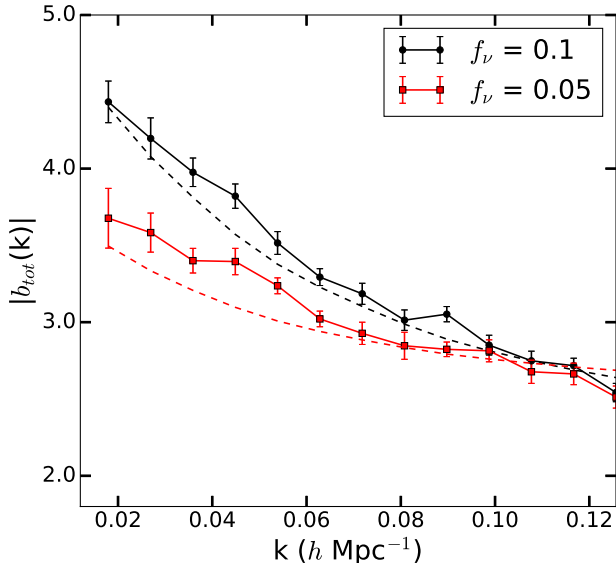


FIG. 18.— Effect of f_ν on the scale-dependent bias using our method for a fixed neutrino mass of $m_\nu = 0.1 \text{ eV}$. We compare the case where $f_\nu = 0.1$ (black) to the case where $f_\nu = 0.05$ (red). The dashed lines show the predictions from the spherical expansion model.

which denote the scatter in the bias from different realizations. As can be seen, treating the neutrinos in a linear approximation leads to an even stronger scale dependence in the bias.

To illustrate how strong this effect is, we also run a set of 8 simulations with CDM only such that the final power spectra closely matches the final power spectra in the simulations with neutrinos. We then use the same void finder on the CDM-only runs to find voids and calculate the linear bias. This is then plotted on the same figure, and shows that it is extremely flat on linear scales.

To study the nature of the scale dependence, we perform a χ^2 fit of the large scale bias from our simulations using Eqn. (46) with $b_{\text{CDM}}(k)$ and $b_\nu(k)$ assumed to be scale independent. For the simulation parameters described above, we find a best-fit value of $b_{\text{CDM}} = -1.91$ and $b_\nu = -3.69$ with $\chi^2/\text{d.o.f}$ value of 0.488. We do a similar fit for the large scale bias obtained from simulations which assumed the neutrinos to be a linear fluid, which showed a stronger scale dependence. In this case we get best-fit values of $b_{\text{CDM}} = -1.94$ and $b_\nu = -3.95$ with $\chi^2/\text{d.o.f}$ value of 0.587. We see b_ν shows a larger difference in the two cases than b_{CDM} . Also, the absolute value of b_ν is larger in the linear approximation, meaning that the voids we have selected are rarer in the linear approximation simulations. In the linear approximation, we truncate the evolution equations at the first order in perturbed quantities like the overdensities and peculiar velocities, and so creating deep voids becomes more difficult.

To obtain an analytic understanding of these results, we use the spherical expansion model (e.g. Fillmore & Goldreich 1984; Jennings et al. 2013), modified to include the effects of massive neutrinos. Firstly, we assume that the ratio of the Lagrangian void biases

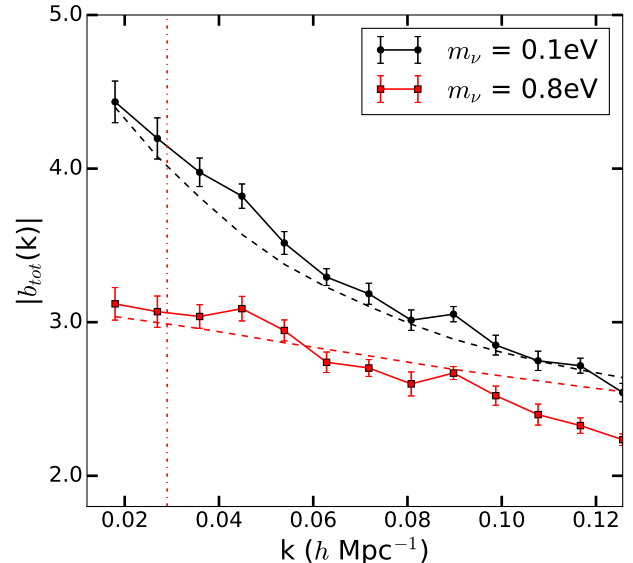


FIG. 19.— Effect of neutrino mass on the scale dependent bias. We compare the bias when the mass of the neutrino is 0.1 eV (black) to the case when the mass is 0.8 eV (red) with $f_\nu = 0.1$ in both cases. The red dot-dashed line gives the free streaming length for the 0.8 eV neutrino. The free streaming length of the lighter neutrino lies outside (to the left of) this plot. The scale dependent bias is evident below the streaming length of each species. The dashed lines show predictions from the spherical expansion model.

b_ν^L and b_{CDM}^L is given by

$$\frac{b_\nu^L}{b_{\text{CDM}}^L} = \frac{f_\nu \frac{d\Delta_{\text{nl}}}{d\delta_{\text{lin}}}|_\nu}{f_{\text{CDM}} \frac{d\Delta_{\text{nl}}}{d\delta_{\text{lin}}}|_{\text{CDM}}} \quad (49)$$

where Δ_{nl} is the actual average nonlinear density of each species enclosed in the voids, while δ_{lin} is the prediction for the average enclosed overdensity from linear theory only. Since the neutrino perturbations are still expected to be small (and therefore close to expectations from linear perturbation theory) in the voids that we studied, we assume that $\frac{d\Delta_{\text{nl}}}{d\delta_{\text{lin}}}|_\nu = 1$.

In the spherical expansion model, we assume that neutrinos form a smooth component, and therefore expand with the background. The CDM component can be thought of as an underdense universe, whose evolution is governed by the Friedmann equation. The time evolution of the scale factor a in the unperturbed background universe follows

$$\left(\frac{da}{dt}\right) = H_0 \left[\frac{1}{a}\right]^{1/2} \quad (50)$$

where H_0 is the present Hubble parameter and we have assumed $\Omega_m = 1$. The perturbed universe, whose scale factor we denote as χ evolves as

$$\left(\frac{d\chi}{dt}\right) = H_0 \left[\frac{f_{\text{CDM}}}{\chi} + \frac{5}{3}f_{\text{CDM}}|\delta| + \frac{\chi^2(1-f_{\text{CDM}})}{a^3}\right]^{1/2} \quad (51)$$

where we have used the fact $f_\nu = 1 - f_{\text{CDM}}$ is a non-clustering component of the total matter density. The nonlinear overdensity of the CDM component at a time

t is

$$\Delta_{\text{nl}}(t) = \left(\frac{a(t)}{\chi(t)} \right)^3 - 1 \quad (52)$$

Eqns. (51) and (50) can be solved to find the average enclosed nonlinear overdensity Δ_{nl} in Eqn. (52) as a function of the linear overdensity δ . This can then be substituted back into the denominator of the right-hand side of Eqn. (49). Once we obtain the Lagrangian biases, we need a prescription to convert to Eulerian biases to compare with the simulation results. This mapping is not straightforward in the presence of a free streaming species, i.e. the neutrinos (LoVerde 2014). As an approximation we assume that the advection of the voids is dominated by the advection of the CDM component, neglecting the effect of the advection of neutrinos. This approximation is equivalent to setting $b_\nu = b_\nu^L$ and $b_{\text{CDM}} = b_{\text{CDM}}^L + 1$, where the value of b_{CDM} is calculated using the best fit to the simulation results. We then compare the ratio of the Eulerian biases from this calculation to the ratio we find in simulations for different void threshold definitions. This comparison is shown in Fig. 16, which demonstrates that this simple model seems to quantitatively explain the trend seen in the simulations, for void definitions using overdensity thresholds in the range -0.5 to -0.8 . Below threshold of -0.8 , there are too few objects in the simulation box to get reliable statistics on the behavior of the bias. We also do not go above -0.5 in the void definition so that the voids we select always have a Lagrangian bias of $\lesssim -2$.

Since most galaxy surveys define voids using galaxy counts, which depend on the underlying CDM field, rather than the total matter field, we investigate the behavior of the bias when we select voids in the simulation using the CDM field only. Once again, we used an enclosed overdensity threshold of -0.7 . We plot $b_{\text{tot}}(k)$ for this sample of voids with the black curve in Fig. 17 and find that it shows very little scale dependence. From this sample of voids selected using the CDM densities only, we split into two subsamples based on the enclosed total matter overdensity - above and below the median value in the sample. When we plot the behavior of $b_{\text{tot}}(k)$ for the two subsamples, (green and red curves in Fig. 17) we find a very strong scale dependence in the biasing. This strategy of identifying voids using the CDM field and then splitting the sample using the total matter field could be used in surveys like DES where both galaxy counts and lensing data is available to search for this scale dependent bias. Here we have not taken into account the noise in the lensing signal, which will, of course, be present in the lensing data from actual surveys. This noise will serve to weaken the differences in the behavior of the biases of the two samples, and in future work we will investigate the effect of lensing noise in washing out the signal shown in Fig. 17.

We also investigated how this scale-dependent linear bias changes as we vary f_ν defined in Eqn. (43). Once again we ran 8 realizations with the same cosmological parameters as above, except for Ω_{CDM} and Ω_ν , for which we used the values 0.285 and 0.015 respectively. This is equivalent to $f_\nu = 0.05$. As seen in Fig.18, this leads to two effects - the voids defined similarly in both sets of simulations have a lower overall amplitude of the bias for the $f_\nu = 0.05$ case, and secondly, the scale depen-

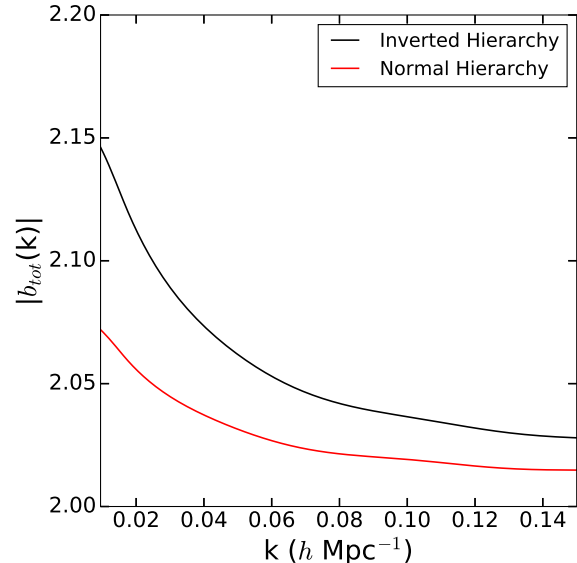


FIG. 20.— Scale dependent bias from the spherical expansion model for inverted hierarchy (black curve) and normal hierarchy (red curve). In the inverted hierarchy, $\sum m_\nu = 0.12 \text{ eV}$, $f_\nu \sim 0.0087$ and $f_{\text{CDM}} \sim 0.9913$. In the normal hierarchy, $\sum m_\nu = 0.06 \text{ eV}$, $f_\nu \sim 0.0043$ and $f_{\text{CDM}} \sim 0.9957$. Voids are defined as regions enclosing an underdensity -0.7 in both cases. We assume that $b_{\text{CDM}} = -2$ for reference.

dence also decreases. This lower bias is a consequence of the lower mass fraction in neutrinos: with smaller f_ν , it is easier to make more voids of the size we consider, and therefore the magnitude of the bias of such objects decreases.

Next, we investigated how the neutrino free streaming scale affects the scale dependence that we observe in the void bias. To do this, we ran a set of 8 simulations for a $m = 0.8 \text{ eV}$ neutrino with $f_\nu = 0.1$. We keep the other cosmological parameters to be the same as earlier. We use such a heavy neutrino species to illustrate how the shape of the void bias is different above and below the free streaming length of the neutrino. For the $m = 0.8 \text{ eV}$, the free streaming scale is about $250 h^{-1} \text{ Mpc}$ - this scale is represented by the dotted red line in Fig. 19. At scales larger than the free streaming scale (smaller k), the CDM power spectrum and the neutrino power spectrum are the same, and there is very little scale dependence in the void bias. On the other hand, at scales below the free streaming scale where the CDM and the neutrino power spectra are significantly different, the bias starts showing a clear scale dependence. This is in contrast to the $m = 0.1 \text{ eV}$ neutrino, for which the free streaming scale is larger than our simulation box and therefore shows a scale dependent void bias at all the scales that we investigate. We also see that the scale dependence is steeper for the lighter neutrino particle - this is because the power spectrum for the lighter neutrino is more damped (and therefore more different from the CDM power spectrum) at any given scale.

While we plan to do a comprehensive study of this scale dependent void bias for realistic ranges of neutrino masses, we can use the spherical expansion model calculation to predict the approximate size of the bias effect for realistic neutrino number densities and minimal masses in the normal hierarchy and the inverted hier-

archy. For the inverted hierarchy case, we assume the minimal sum of the neutrino masses, $\sum m_\nu \approx 0.12$ eV, so that $\Omega_\nu \approx 0.0026$. With the choice of $\Omega_\Lambda = 0.7$, we have $f_{\text{CDM}} \approx 0.9913$ and $f_\nu \approx 0.0087$. In the normal hierarchy, the minimal sum of the neutrino masses is $\sum m_\nu \approx 0.06$ eV, which gives $\Omega_\nu \approx 0.0013$. In this case, $f_{\text{CDM}} \approx 0.9957$ and $f_\nu \approx 0.0043$. We use the spherical expansion model to compute the ratio of the biases b_ν and b_{CDM} , defining voids to be enclosing a total underdensity of -0.7 . We then used linear transfer functions and power spectra at $z = 0$, generated using CLASS, to see how strongly b_{tot} varies as a function of scale on these large scales. We plot the result in Fig. 20 assuming that the voids have $b_{\text{CDM}} = -2$ for reference. From our $f_\nu = 0.1$ simulations, we found that voids with radius about $6 h^{-1}$ Mpc to $8 h^{-1}$ Mpc with an enclosed overdensity threshold of -0.7 had Eulerian biases close to -2 .

To quickly evaluate the ratio of the biases b_ν^L/b_{CDM}^L predicted by the spherical expansion model over the range of realistic values of the neutrino masses as a function of f_ν and the threshold underdensity for void definition, Δ_v , we provide below a fitting function in these variables. We find that

$$\frac{b_\nu^L}{b_{\text{CDM}}^L} \approx A f_\nu^b |\Delta|^c \exp(d|\Delta|) \quad (53)$$

with the best fit parameters $A = 5.37 \times 10^{-6}$, $b = 1.07$, $c = -7.57$ and $d = 16.77$. This fitting formula is accurate to a few percent over the range of $0.001 < f_\nu < 0.025$ and $0.5 < |\Delta| < 0.8$.

7. CONCLUSIONS

In this paper we have presented a novel, hybrid method for performing cosmological simulations in which particles have finite thermal velocities, using hydrodynamics along with standard N-body techniques used in CDM simulations. We have tested our method extensively in both the linear regime, as well as on non-linear problems.

For cosmologies with massive neutrinos, our novel method appears to accurately evolve cosmic structures at all redshifts and all scales, including both linear and nonlinear regimes. This is in contrast to traditional N-body methods, which are known to produce significant errors in the clustering of neutrinos even at low redshift (e.g. Fig. 5). However, for warm dark matter (WDM) cosmologies, we find that the Eulerian version of our method produces too much numerical diffusion to be useful. Instead, we find that using Lagrangian approaches to solving the fluid equations, like smoothed particle hydrodynamics, allows us to circumvent the problem of diffusion on small scales.

We have also presented a novel effect in cosmologies with massive neutrinos - the strong scale dependence in the bias of voids, even on linear scales. These voids were defined using the overall matter fields (CDM and

neutrinos), rather than just the CDM fields. We note that even for voids defined using CDM field only, there is scale dependence in the large scale bias, but that effect is very weak, similar to the dependence seen in the halo bias in Villaescusa-Navarro et al. (2013); LoVerde (2014). For mass-defined halos, the scale dependence of the bias found from our hybrid method matches the results from simulations in which neutrinos were treated as N-body particles to within the error bars. However, linear theory simulations over-predict the strength of the scale dependence. For an inverted mass hierarchy of neutrinos, with $f_\nu \sim 0.01$, we find about 5% scale dependence of the void bias. For the normal hierarchy, the effect is about 2%. A detailed study scanning all of the allowed parameter space in neutrino mass is required to predict how strongly this effect might show up in actual observations. Observationally, voids are normally identified using galaxy counts in surveys (e.g. Sánchez et al. 2016; Clampitt et al. 2016), rather than identification from the lensing shear field. Our results indicate that it may be worthwhile to attempt to detect voids in the mass field directly from lensing, rather than from galaxies, since mass-selected voids should exhibit the neutrino-dependent bias effect discussed above. The other strategy could be to first identify voids using the galaxy counts, and then subdividing the sample based on the mass field, which can be inferred through the gravitational lensing signal. As we have shown, the two subsamples of voids should exhibit scale dependence in their bias.

The simulations presented in this paper used a fixed grid and therefore had low spatial resolution. In the future, we plan to combine our fluid method with adaptive mesh refinement simulation codes, which will allow us to study dark matter halos and galaxies. A particularly interesting area to study is redshift space distortions. The scale dependent growth factor in cosmologies with massive neutrinos is in principle observable in surveys measuring these redshift space distortions. While this effect has been studied using methods like perturbation theory (Upadhye et al. 2016) or N-body techniques (Marulli et al. 2011), it will be interesting to see how the results from our hybrid simulations compare with these other approaches.

We thank Mani Chandra, Charles Gammie, Nickolay Gnedin, Andrey Kravtsov, Marilena LoVerde, and Masahiro Takada for many helpful discussions. We also thank Julien Lesgourgues and Thomas Tram for assistance with the CLASS software. This work was supported by NASA under grant NNX12AD02G. ND was also supported by a Sloan Fellowship, by the Institute for Advanced Study, by the Ambrose Monell Foundation, and by the Center for Advanced Study at UIUC.

REFERENCES

- Ahmad, Q. R., Allen, R. C., Andersen, T. C., et al. 2001, Phys. Rev. Lett., 87, 071301
- Ahn, M. H., Aliu, E., Andringa, S., et al. 2006, Phys. Rev. D, 74, 072003
- Ali-Haïmoud, Y., & Bird, S. 2013, MNRAS, 428, 3375, 1209.0461
- An, F., Bai, J., Balantekin, A., et al. 2012, Physical Review Letters, 108, 171803
- Angulo, R. E., Hahn, O., & Abel, T. 2013, MNRAS, 434, 3337, 1304.2406
- Archidiacono, M., & Hannestad, S. 2016, JCAP, 6, 018, 1510.02907
- Avila-Reese, V., Colín, P., Valenzuela, O., D’Onghia, E., & Firmani, C. 2001, ApJ, 559, 516, astro-ph/0010525

- Behroozi, P., Wechsler, R., & Wu, H.-Y. 2012, Rockstar: Phase-space halo finder, Astrophysics Source Code Library
- Binney, J., & Tremaine, S. 2011, Galactic dynamics (Princeton university press)
- Blas, D., Lesgourgues, J., & Tram, T. 2011, JCAP, 7, 34, 1104.2933
- Bode, P., Ostriker, J. P., & Turok, N. 2001, ApJ, 556, 93, astro-ph/0010389
- Brandbyge, J., & Hannestad, S. 2009, JCAP, 5, 2, 0812.3149
- , 2010, JCAP, 1, 21, 0908.1969
- Brandbyge, J., Hannestad, S., Haugbølle, T., & Wong, Y. Y. Y. 2010, JCAP, 9, 14, 1004.4105
- Carbone, C., Petkova, M., & Dolag, K. 2016, ArXiv e-prints, 1605.02024
- Castorina, E., Carbone, C., Bel, J., Sefusatti, E., & Dolag, K. 2015, JCAP, 7, 043, 1505.07148
- Castorina, E., Sefusatti, E., Sheth, R. K., Villaescusa-Navarro, F., & Viel, M. 2014, JCAP, 2, 49, 1311.1212
- Clampitt, J., Jain, B., & Sánchez, C. 2016, MNRAS, 456, 4425, 1507.08031
- Colberg, J. M., Sheth, R. K., Diaferio, A., Gao, L., & Yoshida, N. 2005, MNRAS, 360, 216, astro-ph/0409162
- Costanzi, M., Villaescusa-Navarro, F., Viel, M., et al. 2013, JCAP, 12, 12, 1311.1514
- Dalal, N., Doré, O., Huterer, D., & Shirokov, A. 2008, Phys. Rev. D, 77, 123514, 0710.4560
- de Blok, W. J. G. 2010, Advances in Astronomy, 2010, 5, 0910.3538
- de Blok, W. J. G., Walter, F., Brinks, E., et al. 2008, AJ, 136, 2648, 0810.2100
- Diemand, J., Kuhlen, M., Madau, P., et al. 2008, Nature, 454, 735, 0805.1244
- Diemand, J., & Moore, B. 2011, Advanced Science Letters, 4, 297, 0906.4340
- Dodelson, S. 2003, Modern cosmology (Academic Press)
- Eguchi, K., Enomoto, S., Furuno, K., et al. 2003, Physical Review Letters, 90, 021802
- Fillmore, J. A., & Goldreich, P. 1984, ApJ, 281, 9
- Fukuda, Y., Hayakawa, T., Ichihara, E., et al. 1998, Phys. Rev. Lett., 81, 1562
- Gao, L., Springel, V., & White, S. D. M. 2005, MNRAS, 363, L66, astro-ph/0506510
- Harten, A. 1983, Journal of computational physics, 49, 357
- Heitmann, K., Ricker, P. M., Warren, M. S., & Habib, S. 2005, ApJS, 160, 28, astro-ph/0411795
- Heitmann, K., Lukić, Z., Fasel, P., et al. 2008, Computational Science and Discovery, 1, 015003, 0706.1270
- Hezaveh, Y., Dalal, N., Holder, G., et al. 2013, ApJ, 767, 9, 1210.4562
- Hezaveh, Y. D., Dalal, N., Marrone, D. P., et al. 2016, ApJ, 823, 37, 1601.01388
- Hobbs, A., Read, J. I., Agertz, O., Iannuzzi, F., & Power, C. 2016, MNRAS, 458, 468, 1503.02689
- Hockney, R. W., & Eastwood, J. W. 1988, Computer simulation using particles (CRC Press)
- Inman, D., Emberson, J. D., Pen, U.-L., et al. 2015, Phys. Rev. D, 92, 023502, 1503.07480
- Jain, B., & Khoury, J. 2010, Annals of Physics, 325, 1479, 1004.3294
- Jenkins, A., Frenk, C. S., White, S. D. M., et al. 2001, MNRAS, 321, 372, astro-ph/0005260
- Jennings, E., Li, Y., & Hu, W. 2013, MNRAS, 434, 2167, 1304.6087
- Klypin, A., Kravtsov, A. V., Valenzuela, O., & Prada, F. 1999, ApJ, 522, 82, astro-ph/9901240
- Lesgourgues, J. 2011, ArXiv e-prints, 1104.2932
- Lesgourgues, J., & Pastor, S. 2014, New Journal of Physics, 16, 065002, 1404.1740
- Lesgourgues, J., & Tram, T. 2011, JCAP, 9, 32, 1104.2935
- LoVerde, M. 2014, Phys. Rev. D, 90, 083530, 1405.4855
- , 2016, Phys. Rev. D, 93, 103526, 1602.08108
- Marulli, F., Carbone, C., Viel, M., Moscardini, L., & Cimatti, A. 2011, MNRAS, 418, 346, 1103.0278
- Massara, E., Villaescusa-Navarro, F., Viel, M., & Sutter, P. M. 2015, JCAP, 11, 018, 1506.03088
- Mo, H., van den Bosch, F. C., & White, S. 2010, Galaxy Formation and Evolution
- Monaghan, J. J. 1992, ARA&A, 30, 543
- Moore, B., Ghigna, S., Governato, F., et al. 1999, ApJ, 524, L19, astro-ph/9907411
- Navarro, J. F., Frenk, C. S., & White, S. D. M. 1997, ApJ, 490, 493, astro-ph/9611107
- Peebles, P. J. E. 1980, The large-scale structure of the universe
- Planck Collaboration, Ade, P. A. R., Aghanim, N., et al. 2014, A&A, 571, A16, 1303.5076
- Roe, P. 1986, Annual review of fluid mechanics, 18, 337
- Sánchez, C., Clampitt, J., Kovacs, A., et al. 2016, ArXiv e-prints, 1605.03982
- Scherrer, R. J., & Weinberg, D. H. 1998, ApJ, 504, 607, astro-ph/9712192
- Springel, V. 2005, MNRAS, 364, 1105, astro-ph/0505010
- Springel, V., White, S. D. M., Jenkins, A., et al. 2005, Nature, 435, 629, astro-ph/0504097
- Springel, V., Wang, J., Vogelsberger, M., et al. 2008, MNRAS, 391, 1685, 0809.0898
- Stadel, J., Potter, D., Moore, B., et al. 2009, MNRAS, 398, L21, 0808.2981
- Tinker, J., Kravtsov, A. V., Klypin, A., et al. 2008, ApJ, 688, 709, 0803.2706
- Tinker, J. L., Robertson, B. E., Kravtsov, A. V., et al. 2010, ApJ, 724, 878, 1001.3162
- Toro, E. F. 2009, Riemann solvers and numerical methods for fluid dynamics: a practical introduction (Springer Science & Business Media)
- Upadhye, A., Kwan, J., Pope, A., et al. 2016, Phys. Rev. D, 93, 063515
- Van Leer, B. 1977, Journal of computational physics, 23, 276
- Villaescusa-Navarro, F., Bird, S., Peña-Garay, C., & Viel, M. 2013, JCAP, 3, 19, 1212.4855
- Villaescusa-Navarro, F., & Dalal, N. 2011, JCAP, 3, 24, 1010.3008
- Villaescusa-Navarro, F., Marulli, F., Viel, M., et al. 2014, JCAP, 3, 11, 1311.0866
- Villaescusa-Navarro, F., Vogelsberger, M., Viel, M., & Loeb, A. 2011, ArXiv e-prints, 1106.2543
- Wang, J., & White, S. D. M. 2007, MNRAS, 380, 93, astro-ph/0702575
- Warren, M. S., Abazajian, K., Holz, D. E., & Teodoro, L. 2006, ApJ, 646, 881, astro-ph/0506395
- Zemp, M. 2009, Modern Physics Letters A, 24, 2291, 0909.4298